T.C.
IZMIR DEMOKRASI UNIVERSITY
GRADUATE SCHOOL OF NATURAL AND APPLIED SCIENCES

MASTER THESIS
ELECTRICAL AND ELECTRONICS ENGINEERING DEPARTMENT

ANALYSIS OF WOUND HEALING ASSAY DATA OF PHASE-CONTRAST OPTICAL MICROSCOPY USING TRADITIONAL COMPUTER VISION AND DEEP LEARNING TECHNIQUES

by
Yusuf Sait ERDEM
ORCID: 0000-0002-8515-8303

Supervisor:
Prof. Dr. Devrim ÜNAY

Co-Supervisor:
Prof. Dr. Behçet Uğur TÖREYİN

İZMİR–2023

THESIS APPROVAL

The thesis named "**Analysis of Wound Healing Assay Data of Phase-Contrast Optical Microscopy Using Traditional Computer Vision and Deep Learning Techniques**" is prepared by **Yusuf Sait ERDEM** was successfully defended as a **MASTER'S THESIS** on 25/07/2023 in front of the following jury members at İzmir Democracy University, Institute of Science and Technology, **Department of Electrical and Electronics Engineering Department.**

Supervisor:	**Prof. Dr. Devrim ÜNAY** İzmir Demokrasi University
Committee Member:	**Prof. Dr. Devrim PESEN OKVUR** İzmir Institute of Technology
Committee Member:	**Dr. Başak Esin KÖKTÜRK GÜZEL** İzmir Demokrasi University

COMMITMENT

I hereby declare that this thesis has been written at the Graduate School of Natural and Applied Sciences at Izmir Democracy University in accordance with academical and ethical rules and all the literature informations that is used in this thesis mentioned references.

Yusuf Sait ERDEM

CONTENTS

LIST OF ICONS AND ABBREVIATIONS

AdaIN	Adaptive Instance Normalization
C-GAN	Conditional Generative Adversarial Network
CIV	Cell Image Velocimetry
DSSIM	Distance Structural Dissimilarity Index Measure
FID	Fréchet Inception Distance
GANs	Generative Adversarial Networks
MS-SSIM	Multiscale Structural Similarity
MSD	Mean Surface Distance
NST	Neural Style Transfer
PCM	Phase-Contrast Microscopy
PSNR	Peak Signal-to-Noise Ratio
ReLU	Rectified Linear Activation Unit
SLF	Supplementary Loss Function
SSIM	Structural Dissimilarity Index Measure

LIST OF FIGURES

LIST OF TABLES

Page

ACKNOWLEDGMENTS

To my advisor, Prof. Dr. Devrim ÜNAY, who supported and guided me professionally and kindly at every stage of my work. To my dear co-advisor, Prof. Dr. Behçet Uğur TÖREYİN, who enlightened me with his experiences and knowledge. To Scientific and Technological Research Council of Turkey (TUBITAK), which supported this project under grant no 119E578. To my team members from the Tubitak project, which was very enlightening and rewarding experience to collaborate with. I would like to express my deep gratitude to my family, who have consistently supported me morally throughout my educational journey and always standed by my side.

The data used in this study is collected under the Marie Curie IRG grant (no: FP7 PIRG08-GA-2010-27697).

Yusuf Sait ERDEM
İzmir, 2023

ABSTRACT

Master's Thesis

Analysis of Wound Healing Assay Data of Phase-Contrast Optical Microscopy Using Traditional Computer Vision and Deep Learning Techniques

Yusuf Sait ERDEM

İzmir Demokrasi University
Graduate School of Natural and Applied Sciences
Electrical and Electronics Department

Supervisor: Prof. Dr. Devrim ÜNAY

Co-Supervisor: Prof. Dr. Behçet Uğur TÖREYİN

This thesis aims to investigate the performances of image segmentation and image synthesis methods applied to wound healing assay data, and propose novel solutions to improve accuracies. For segmentation, the utilization of both traditional and deep-learning approaches is studied in various scenarios. Additionally, the thesis addresses the challenge of limited training data commonly encountered in biomedical research. To overcome this problem, methods for generating synthetic assay data is explored. The comparative analysis and demonstration of these methods are performed over a phase-contrast optical microscopy time-series dataset of wound healing assays.

While classical computer vision techniques have been widely used for segmentation of wound healing assay images, there is a scarcity of studies focusing on solutions based on recently emerged deep learning techniques. Therefore, this thesis examines traditional segmentation methods in addition to the investigation of the segmentation capability of deep learning solutions to provide improved analysis and quantification of wound healing assays. Moreover, efficient methods for generating synthetic assay data are explored to improve the segmentation performance of deep learning methods, particularly in situations where training data are limited which is often encountered in biomedical research.

Keywords: Image segmentation, computer vision, deep learning, medical data synthesis, phase-contrast microscopy data, wound healing assay data analysis

2023, 47 pages

ÖZET

Yüksek Lisans Tezi

Geleneksel Bilgisayarda Görü ve Derin Öğrenme Teknikleri Kullanılarak Faz Kontrast Optik Mikroskopi Yara İyileşmesi Deney Verilerinin Analizi

Yusuf Sait ERDEM

İzmir Demokrasi Üniversitesi
Fen Bilimleri Enstitüsü
Elektrik - Elektronik Mühendisliği Anabilim Dalı

Danışman: Prof. Dr. Devrim ÜNAY

II. Danışman: Prof. Dr. Behçet Uğur TÖREYİN

Bu tez, yara iyileşme deneyi verileri için görüntü bölütleme ve görüntü sentezleme yöntemlerinin başarımlarını araştırmayı amaçlamaktadır ve başarımları iyileştirmek için yeni yöntemler önermektedir. Bölütlemede, farklı durumlarda kullanabilmek için, geleneksel ve derin öğrenme yaklaşımları incelenmiştir. Ayrıca, biyomedikal araştırmalarda sıkça karşılaşılan işaretli eğitim verisetlerinin sınırlı olması durumuna da değinilmektedir. Bu sorunu aşmak için sentetik deney verisi oluşturma yöntemleri incelenmiştir. Bu yöntemlerin karşılaştırmalı analizi, yara iyileşme deneylerinin faz kontrastlı optik mikroskopi zaman serisi veriseti kullanılarak gerçekleştirilmektedir.

Klasik bilgisayarlı görme teknikleri, yara iyileşme deneyi görüntülerinin bölütlenmesinde yaygın bir şekilde kullanılmaktadır. Ancak bu alanda, son zamanlarda yaygınlaşan derin öğrenme tekniklerine dayalı çalışmaların eksikliği bulunmaktadır. Bu nedenle bu tez, yara iyileşmesi deneylerinin daha hassas analizi ve nicelleştirilmesi için geleneksel bölütleme yöntemlerini incelemenin yanı sıra, derin öğrenme çözümlerinin bölütleme yeteneklerini de araştırmaktadır. Ayrıca, biyomedikal çalışmalarda sıkça karşılaşılan eğitim verisin sınırlı olması durumunda, derin öğrenme yöntemlerinin bölütleme performansını iyileştirmek için etkili sentetik deney verisi oluşturma yöntemleri de araştırılmıştır.

Anahtar Kelimeler: Görüntü bölütleme, bilgisayarlı görü, derin öğrenme, medikal veri sentezi, faz-kontrast miksorkopi verisi, yara iyileşmesi veri analizi

2023, 47 sayfa

1. INTRODUCTION

Wound healing assays are essential tools in biomedical research, providing valuable data for understanding the complex process of cell migration. Accurate analysis and quantification of wound healing assays is important in research topics such as the study of cellular responses to various stimulus, understanding the cell-to-cell interactions, and exploration of cell migration mechanisms.

Imaging techniques, such as phase-contrast or fluorescent microscopy, are employed for acquiring data from wound healing assays. Among these techniques, phase-contrast imaging is preferable for being less harmful, making it more suitable for studying living specimens. However, accurately segmenting objects of interest from phase-contrast microscopy images can be challenging due to less highlighted boundaries of the subjects.

Advancements in automated microscopy techniques has greatly helped in generating large amounts of data efficiently from wound healing experiments. However, manual segmentation of this large amount of data is laborious, time-consuming, and affected by subjective style variation, leading to inconsistent results. As a result, automated segmentation techniques have gained popularity as they offer more efficient and reliable solutions for analyzing wound healing data.

The literature on segmentation of wound healing assays can be categorized into two main approaches: traditional methods and deep learning-based methods. Traditional methods have the advantage of not requiring excessive computational resources or long computation times. However, they usually require parameter to be tuned manually and thus they are more difficult to generalize for different conditions. In contrast, the recently emerged deep learning methods achieve higher accuracies and they are better at generalization in segmentation tasks. However, they require significant computational power (or longer processing times) and a substantial amount of annotated data for training. Advantages and disadvantages of both approaches in terms of performance and resource requirements need to be considered when selecting the appropriate method for the task at hand.

In this thesis, traditional and deep learning based segmentation methods for wound healing assay data are studied, and novel solutions are proposed to achieve improved performance. In addition to the investigation of wound healing assay data segmentation methods, the challenge of limited training data is also addressed which is commonly encountered in biomedical research. To overcome this difficulty, methods for generating synthetic assay data are explored, compared and showcased using a wound healing assay time-series dataset of phase-contrast optical microscopy.

2. GENERAL INFORMATION / RELEVANT LITERATURE

2.1. Wound Healing Assay

Wound healing assays provide information about mechanisms governing collective cell migration which is essential for analysis of biological topics such as immune system activation, growth of the tumor, and metastasis as well as embodiment of tissues. As a result, this technique stands as a fundamental method for molecular biologists.

In typical procedure of wound healing assays, the confluent monolayer of the subject cells is scratched to produce open wound area. Then, the cells are observed while they migrate to close the gap [1, 2]. The process of the cells closing the wound area can be observed via various methods. Two popular solutions that are utilized are time-lapse imaging with phase-contrast microscopy (PCM) and fluorescence microscopy. In fluorescence microscopy, cellular structures are highlighted by labeling with fluorescent stains. On the other hand, this labeling procedure may change behavior of the subject cell or harm the cells due to electromagnetic radiation [3, 4]. In contrast, in PCM light is used to observe cellular structures without using staining/labeling on the specimen, thus it constitutes a safer alternative.

2.2. Semantic Segmentation

For the analysis of PCM images of wound healing assays, accurate segmentation of the wound front is a necessity. Manual annotation of the wound front may be inconvenient since it is time-consuming and annotator-dependent. Thus automated, fast, and robust segmentation solutions are needed.

In literature, methods frequently utilized for cell segmentation in PCM images can be grouped into two as traditional image processing based approaches and methods based on deep-learning. While the deep-learning methods require plenty of training data together with excessive amount of computational resources, the traditional methods may require careful tuning of some parameters for accurate segmentation of the cells.

2.2.1. Traditional Approaches

For the segmentation of wound healing assays, there are some frequently employed methods by biomedical researchers such as Cell Image Velocimetry (CIV) [5] and MRI Wound Healing Tool macro which is an ImageJ macro [6]. To achieve a precise segmentation result when using the CIV segmentation method, the user should set parameters such the kernel size, the local contrast normalization radius, and local and global filtering thresholds. In the MRI Wound Healing Tool plugin, users should not only select their preferred technique but also fine-tune the parameters such as the radius of the structuring element utilized in the morphological opening, and the minimum wound size.

To segment wound healing assay data, in TScratch wound analysis tool by Gebäck - Tobias et al., curvelet transformation with morphological operations are combined [7]. First, a curvelet magnitude image is created by using two scale-levels and morphological opening operation is applied. The scale-level parameters are automatically found or can be tuned for making the margins of the wound apparent. Then, two peak areas on the curvelet histogram are assumed to be true edges, while the rest are discarded as noise edges. Further morphological operations applied for improving the resulting segmentation image.

In another method for analysis of wound healing assays, Matsubayashi et al.'s ‘White wave’ method [8] offers a different approach by analyzing the wound closure in place of direct frontier distance calculations for analysis of wound healing assays. Histogram of the vertical average pixel intensity difference values is generated for consecutive frames. Then the positions of the edges of the wound are identified by the horizontal (x) coordinates of two histogram average intensity values that peaked. According to Matsubayashi et al., the use of average value for wound fronts is more reliable and carries more information than direct frontier distances.

There are various other methods proposed in the literature for segmentation of the wound healing assays involving morphological operations additional to various traditional computer vision techniques such as entropy filtering, variance filtering, and contrast enhancement and adaptive binarization [9 – 12].

Under certain circumstances, these methods are effective, but they rely on a multitude of critical parameters including the kernel size [10, 11, 13], saturation rate [9, 10], scale-level [7], and kernel average percentage threshold [13]. Requirement of human interaction to choose the suitable parameter set to obtain a decent level of precision and consistency under variety of settings, makes these methods cumbersome to apply in practice.

2.2.2. Deep-Learning

In addition to traditional computer vision techniques, deep-learning based methods are also used for the segmentation of wound healing assays, which have emerged as a powerful and versatile tool for deriving meaningful information from complex and imprecise data. Deep learning methods have higher accuracy compared to traditional methods in various problems, but they require a significant amount of (accurately annotated) training data and computational resources. However, since the analysis of wound healing images does not require real-time processing, deep learning methods are efficient in such applications when a sufficient amount of training data is available.

Ronneberger et al. introduced U-Net and demonstrated its efficacy by applying it to the task of segmenting individual cells in phase-contrast microscopy images. The architecture of U-Net illustrated in Figure 2.2.2.1. consists of a contracting path and an an expanding path. The contracting path has a number of blocks with 3x3 convolutions, followed by rectified linear activation unit (ReLU) and 2x2 max pooling. The number of channels is doubled while the size of the feature maps is reduced by half at each step. In the expanding path, while the feature map sizes are doubled with up-sampling operation, a 2x2 convolution halves the number of channels. Then concatenation with corresponding feature maps from the contracting path, and two 3x3 convolutions with ReLU activation are applied at each step.

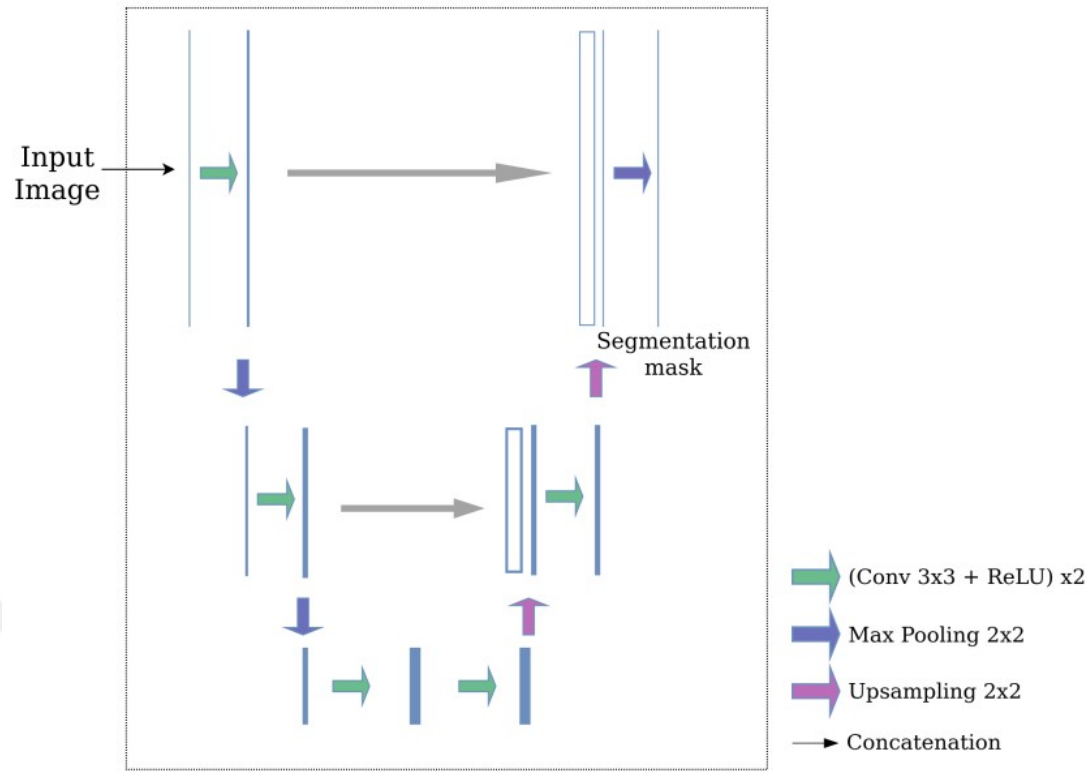

Figure 2.2.2.1. Structure of the U-Net model (adapted from [Ronneberger et al., 2015]).

Mahmud et al. [14] utilized a shallow U-Net with only 1 encoding and 1 decoding steps for blood pressure prediction from photoplethysmogram and electrocardiogram signals. Through a more lightweight version of the U-Net model, they were able to achieve superior performance compared to a majority of existing approaches in a more resource-efficient manner.

Vaswani et al. [15] introduced “attention” mechanism in neural networks. The attention mechanism allows the neural network to focus more on the relevant parts of the input data, while reducing signal activation on irrelevant parts which is expected to enhance the efficiency of the model. Oktay et al. [16] applied this methodology on a U-Net and demonstrated its efficacy on biomedical image segmentation.

The U-Net model is also employed for the segmentation of wound healing assay images [17]–[19]. Mayalı et al. [17] utilized the U-Net model for segmentation

of collective cell regions in phase-contrast images of wound healing assays for the first time. Javer et al. [18] and Oldenburg et al. [19] also utilized U-Net for segmentation of wound healing images. Different from Mayalı et al., in the latter two methods the cells are segmented individually and morphological operations are applied after for obtaining cell cluster regions from fluorescence microscopy images.

2.3. Deep-Learning for Data Generation

Deep learning-based methods have gained great success and popularity in many image processing tasks such as object detection [20], classification [21], segmentation [22], and depth-estimation [23]. The availability and diversity of large amounts of annotated training data are one of the determinants of the effectiveness of deep learning methods. However, in medical-related tasks the shortage of such data is commonplace due to issues associated with data sharing, variation in data acquisition methods, and the requirement of expert knowledge when it comes to data annotation. Data augmentation by creating slightly modified copies of already existing data or by generating new synthetic data from existing data is a solution when there is a lack of sufficient training data. The former is the most preferred approach as it is easy to apply, but such small modifications may bring little additional information. To the contrary, the latter is a more sophisticated approach that may generate semantically more meaningful examples and thus enable more variability and richness in the training dataset [24].

Realistic synthesis of artificial data has become widespread in many fields [25]–[27] especially by the introduction of Generative Adversarial Networks (GANs) by Goodfellow et al. [28]. In GANs, outputs of the synthetic data generator are evaluated by another deep neural network. This discriminator network is trained together with the generative network to learn if the given input is real or artificially generated by comparing the outputs of the generative network and the real data. While the generative network learns to generate more realistic data via feedback from the discriminator network, the discriminator learns to distinguish generated data from the real one.

Isola et al. [26] introduced an image-to-image translation method, Pix2pix, utilizing a conditional GAN (C-GAN), where an additional constraint on the input is

used in both the generation and discrimination steps of a GAN model. They used a U-Net [29] based structure for the generator and PatchGAN [30] for the discriminator of the C-GAN model. In addition to the discriminator's objective function in the C-GAN, L1 distance between the generated data and the real input is utilized as an additional term in the C-GAN loss function. Finally, to synthesize images in a more stochastic manner, dropout operations were applied on some layers of the generator network. The authors stated that, this strategy made little impact and applying noise in the input directly had even less of an impact on the output.

Karras et al. [31] proposed a novel generator architecture using GANs for data generation. In this method, they utilized a GAN model by inserting noise input into feature layers together with learned special scaling factors to improve stochasticity. They also used AdaIN layers, initially employed in Huang et al.'s Neural Style Transfer (NST) method [32], in each feature layer.

In an NST framework, the input comprises of a content image and a style image. The NST method aims to combine the style input's low-level features with the high-level semantic features of the content input using an artificial neural network. It was initially proposed for artistic style transfer [32], [33], but then utilized for other image processing tasks such as source adoption [34], [35], and data augmentation [36]–[40]. Mikołajczyk et al. [40] utilized NST for transferring styles of different kinds of skin lesion images. Cicalese et al. [37] adopted a similar method for histopathology images. Zheng et al. [38] and Jackson et al. [39] both introduced data augmentation with style transfer at the same time. They both used style transfer for augmenting arbitrary object images using chosen style images. Jackson et al. [39] further utilized style embedding instead of a style image input. Likewise, Yamashita et al. [36] utilized NST for augmenting histopathology images using various images from different domains as style inputs.

Deep learning has also been utilized for synthesizing time-lapse microscopy images before. These solutions are validated on two popular microscopy imaging techniques that allow time-lapse acquisition; phase-contrast microscopy (PCM) and fluorescence microscopy. Theagarajan et al. [41] synthesized PCM images of single cells and confined cell clusters in different classes unconditionally using GAN. Bailo

et al. [42] generated bright-field microscopy images of blood cell clusters by first generating locations for each cell. They modeled the distribution of the cells in the cell clusters by considering cell adhesion via a mathematical formula, then synthesized realistic cell images utilizing a Pix2pixHD [43] model, which is a C-GAN method. Fu et al. applied a similar procedure before, by randomly generating ellipses as spatial constraints for the generation of 3D biological structures, captured by fluorescence microscopy [44]. They proposed a spatially constrained CycleGAN model for the final image synthesis step by modifying the CycleGAN structure. While Goldsborough et al. [45] utilized GANs for the synthesis of fluorescent microscopy images of single cells, Baniukiewicz et al. [46] adopted C-GANs by using manual segmentation masks as spatial constraints for a similar task.

We conducted an attribute-based comparison of various prominent methods applied to PCM data generation as shown in Table 2.2.3.1, to point out the novelty of our method.

Table 2.2.3.1. Attribute-based comparison of prominent methods and the proposed method.

Method	Type	Conditional Normalization Layer	Noise Input	Patch Based	Conditional Data Generation
Huang et al. [16]	NST	AdaIN	-	Yes	No
Isola et al. [17]	GAN	-	in a single layer	No	Yes
Karras et al. [28]	GAN	AdaIN	in multiple layers	No	Yes
Proposed	NST	AdaIN	in a single layer	Yes	Yes

The contributions of this study are as follows. We utilized an NST-based method different from the existing solutions proposed for data generation, as shown in Table 3.2.2.1, since GANs have more complex structures and are difficult to train due to adversarial training [25], [28], [47]. Furthermore we have used a patch-based

training method in order to process images in higher resolution with limited memory, benefiting from the nature of the cell clusters that are atomic only in small regions. Also, we provided noise input to the network for increasing the stochasticity in the generated data.

Wound healing assays provide valuable information for biomedical researchers. Classical computer vision techniques can be employed for segmentation of the assay images which is utilized for simpler and reliable analysis of the wound healing assays. Although there are some studies focused on automated analysis of wound healing assay time-series images by using classical image processing techniques, solutions based on the recent and emerging deep learning techniques are scarce. Accordingly, the purpose of this thesis is to examine the segmentation capability of such solutions toward improved precision on analysis and quantification of wound healing assays from phase-contrast optical microscopy time-series images. Additionally, it seeks to investigate efficient ways of generating synthetic assay data for contributing to the segmentation performance of deep learning methods in situations where there is a scarcity of training data and computational resources.

3. MATERIALS AND METHODS

3.1. Wound Healing Assay Data

Wound healing assays are conducted for the acquisition of phase-contrast time-lapse images. Breast cancer cell line MCF7 (7.5×10^5 cells per well) and normal breast cell line MCF10A (1×10^6 cells per well) were seeded on 12-well plates. 24 hours after the seeding, when they reached to confluency, the cells were treated with 10µg/ml mitomycin C for two hours, to prevent proliferation. Then, mitomycin C containing medium was replaced with serum-free medium and the scratch was introduced with a 10µl pipette tip. The cells were placed in the incubation chamber and observed with Leica DMI8 confocal microscope for two days at 37°C with 5% CO_2. The phase contrast images of three positions per well were captured once every hour.

In total, in this study 328 images from 14 wound healing assays were used. The images are stored in 8-Bit, grayscale, TIFF format with 1920×1440 pixel resolution. Some samples from the dataset are depicted in Figure 3.1.1.

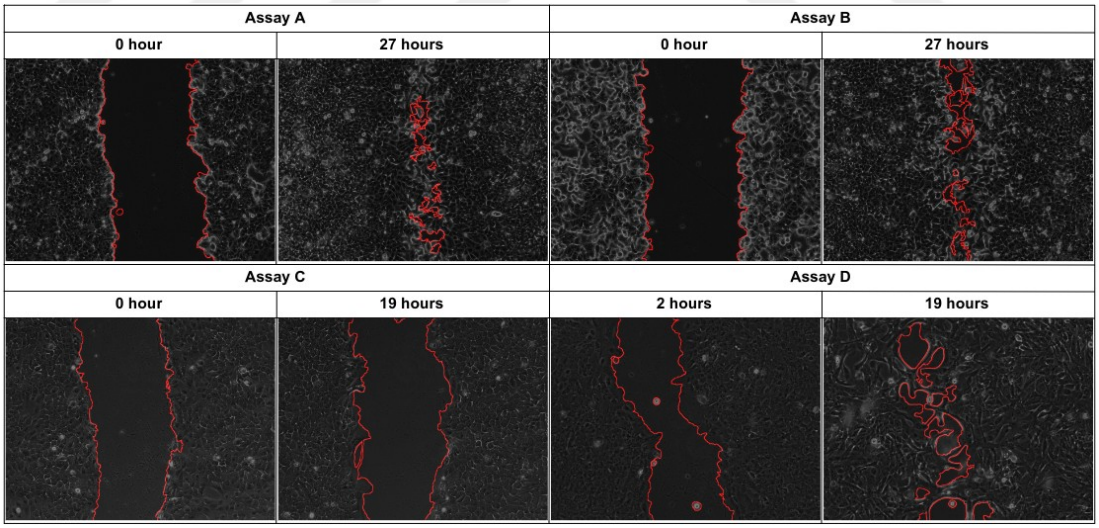

Figure 3.1.1. Sample images from the phase-contrast wound healing assay dataset where the boundaries of the wound fronts manually segmented by experts are overlaid in red. The images are sampled from different time-lapse imaging sets (assays) in the dataset, indicated by A, B, C, and D. Samples correspond to the start and end frames of each assay.

The wound healing assay images were manually annotated using the ImageJ [6] manual annotation and Supervisely [48] online annotation tools under the guidance of field experts. The acquired assay images and annotation masks are 1920×1440 pixels in size. The annotations correspond to the frames starting from the time-point where cell adhesion is realized until the wound closure is completed in each time-lapse microscopy image of every wound healing assay.

All models are trained and tested on a laptop with an NVIDIA GeForce GTX 1650 GPU with 4GBs of GPU memory.

3.2. Methods

3.2.1. Semantic Segmentation

Semantic image segmentation refers to the process of dividing an image into regions or segments for content analysis which is a fundamental task in computer vision. This process identifies boundaries around regions of interest, enabling further analysis and manipulation of visual content. Segmented images allow computer vision systems to extract specific objects, features, or regions which is a crucial step for analysis of the content data. In this thesis, two methods are proposed for the two primary approaches to semantic segmentation of wound healing assay images: traditional computer vision and deep-learning.

3.2.1.1. Traditional Computer Vision Method

In this section, a new method based on traditional computer vision techniques is described for segmentation of wound fronts in the wound healing assays. By employing a combination of well-established traditional computer vision-based operations, such as variance filtering and morphological operations, the method aims to achieve accurate and reliable segmentation results. The flowchart of the method is demonstrated in the Figure 3.2.1.1.1.

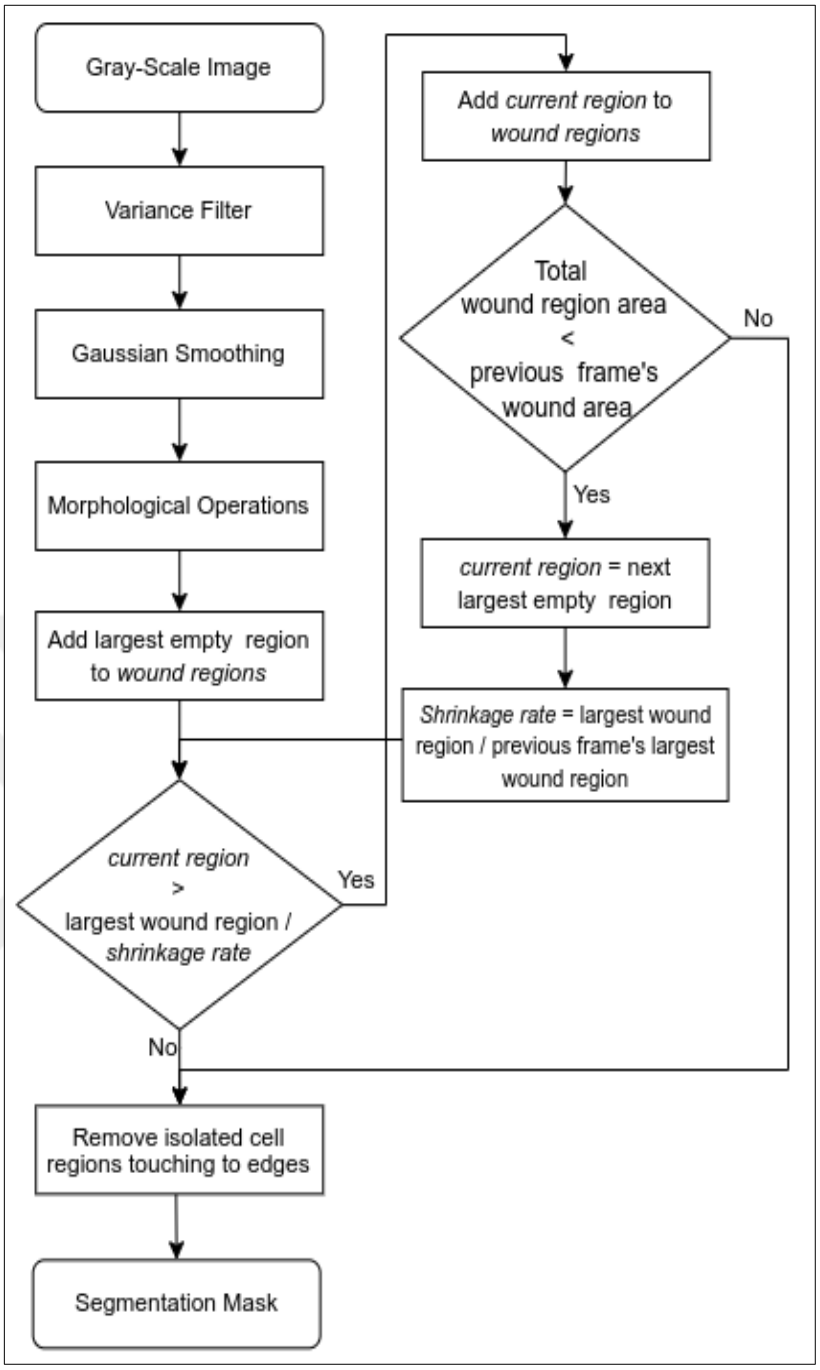

Figure 3.2.1.1.1. Flowchart of the proposed wound healing assay data segmentation method based on traditional computer vision approach.

For segmentation of the wound healing assay images, at first, variance filtering is applied on the gray-scale images of wound healing assays. Then, Gaussian smoothing operation is applied using a kernel with a predetermined kernel size of 25×25. The determination of the kernel size parameter is based on the approximate pixel length of a cell in the input image. The resulting image is

binarized by taking negative values as zeros and positive values as ones. In order to remove small, occupied regions a dilation operation is applied followed by an erosion operation. The resulting image includes empty wound regions as zeros and occupied cell regions as ones. Later, small regions touching to the edges of the frame are eliminated as in the method of Zordan et al. [9]. For the first frame of the wound healing assay time series, all regions are considered as cell regions except for the largest wound region. For the subsequent frames, the remaining zero regions are not explicitly labeled as wound regions, but they are considered as potential wound regions.

In the binary image, for determination of the small regions as wound region or not, temporal information is taken into account. The zero regions are initially sorted based on their sizes. A *shrinkage rate* is calculated by dividing the biggest empty region in the current frame to the biggest empty region of the previous frame. The current biggest empty area is multiplied by the shrinkage rate. If a region in the subsequent frames has a size larger than this calculated area, it is considered as a wound region candidate. These candidate regions are assigned as wound regions starting from the biggest to smallest. Candidate regions are no longer assigned as wound regions if the total wound region exceeds the previous total wound region. This step is applied by considering that, in a wound healing assay the wound region shrinks over time.

3.2.1.2. Deep-Learning Method

The U-Net convolutional neural network is a well-known and precise method for segmenting medical images, and therefore it is applicable for accurate segmentation of phase-contrast microscopy wound healing assay data. However, when dealing with large inputs (for example 1024×1024 or higher sized images), the computational requirements of the U-Net structure increases exponentially. While several approaches have been developed to utilize U-Net models with limited resources, such as down-sampling or tiling the input data, these methods may decrease the accuracy of the results or be impractical for data with large atomic characteristics, like wound healing assay images. In this study, a low-cost and accurate segmentation method for high-resolution wound healing assay time-series

images is examined by utilizing a shallow U-Net structure with a high-resolution input as depicted in the Figure 3.2.1.2.1.

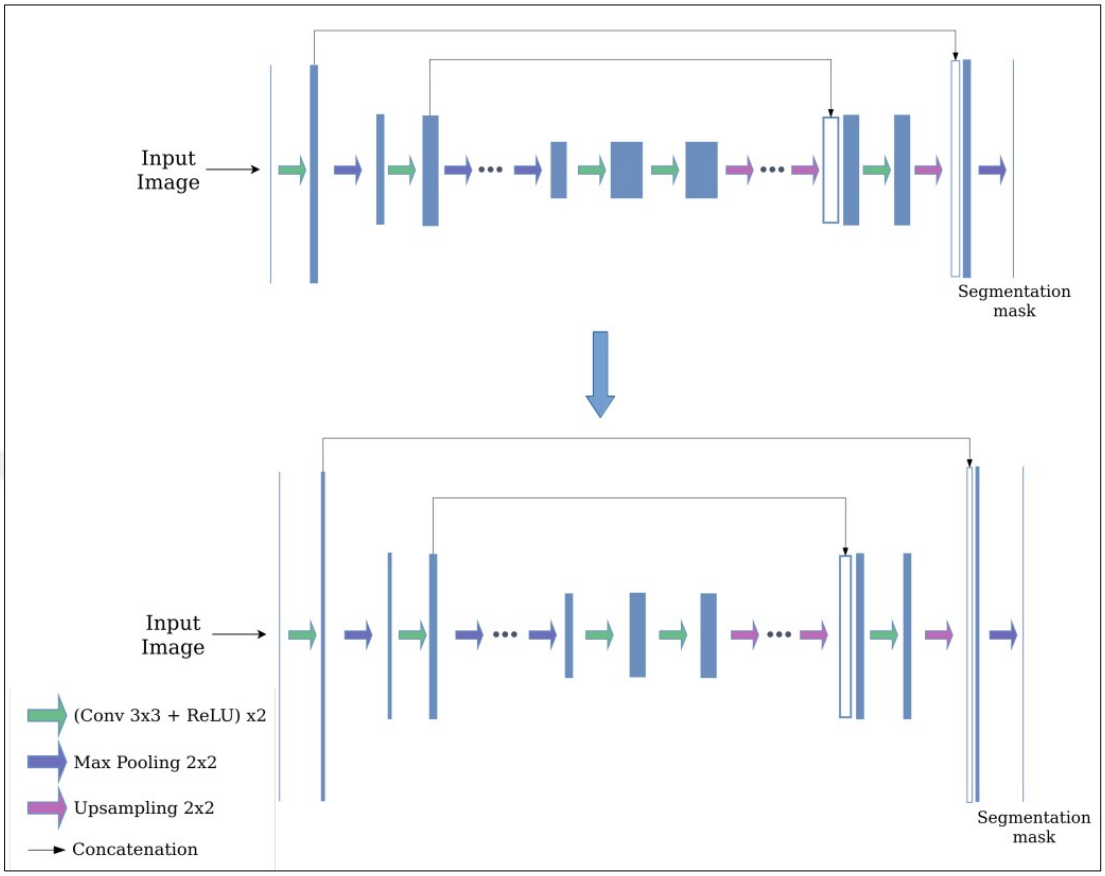

Figure 3.2.1.2.1. Structures of the original U-Net model (top) and the proposed shallower U-Net model (bottom) where the size of the generated feature maps are increased by decreasing the number them in each layer.

To address the challenge of training with high-resolution images under resource constraints, some modifications were introduced to the U-Net architecture similar to Mahmud et al. [14], who used a single-level U-Net structure for resource efficiency. However, unlike Mahmud et al.'s method in this study the sizes of the feature maps are augmented while simultaneously decreasing the number of generated feature maps to maintain optimal memory usage instead of decreasing encoding and decoding steps to one. The number of convolutional layers is further reduced to minimize the number of feature maps as shown in the Figure 3.2.1.2.1.

These modifications enabled to enhance the resolution of the inputs and outputs of the segmentation model from 256×256 pixels to 512×512 pixels.

3.2.1.3. Metrics

To evaluate the segmentation accuracy achieved by the methods under investigation, the Dice coefficient is employed. It is calculated as follows:

$$DiceScore\left(R_{\text{Pred}}, R_{\text{GT}}\right) = \frac{2 * \left|R_{\text{Pred}} \cap R_{\text{GT}}\right|}{\left|R_{\text{Pred}}\right| + \left|R_{\text{GT}}\right|} \quad (1)$$

where R_{Pred} represents the predicted pixel regions and R_{GT} refers to the ground truth regions.

As part of the quantification process, in addition to the proportion of the open wound region's area, the extent of wound closure during the experiment is determined by the Mean Surface Distance which is calculated for the detected wound surfaces at each frame. The Mean Surface Distance measures the average distance between two surfaces by taking the minimum distances across surfaces into account as given below:

$$MSD\left(Surf\,1, Surf\,2\right) = \frac{1}{N_{Surf\,1} + N_{Surf\,2}} \left(\sum_{i=1}^{N_{Surf\,1}} \left| d_i^{Surf\,1 \rightarrow Surf\,2} \right| + \sum_{i=1}^{N_{Surf\,2}} \left| d_i^{Surf\,2 \rightarrow Surf\,1} \right| \right) \quad (2)$$

where Surf1 and Surf2 represent the surfaces of the opposing wound regions, N_{Surf1} and N_{Surf2} denote the point counts of the surfaces, and *d* represents the Euclidean pixel distances in 2D.

An MSD-based wound front distance measurement method is proposed to quantify wound healing assay time-series images. Two opposite wound fronts are detected to measure MSD in between them. At first, a rotated bounding box is fitted into each wound region. A mid-line is drawn towards the longitude of the bounding box and two tip points of the lines are taken. Then the wound surface is separated

into from two points on the surface line where they are closest points to the taken points from the previous step as shown in the Figure 3.2.1.3.1.

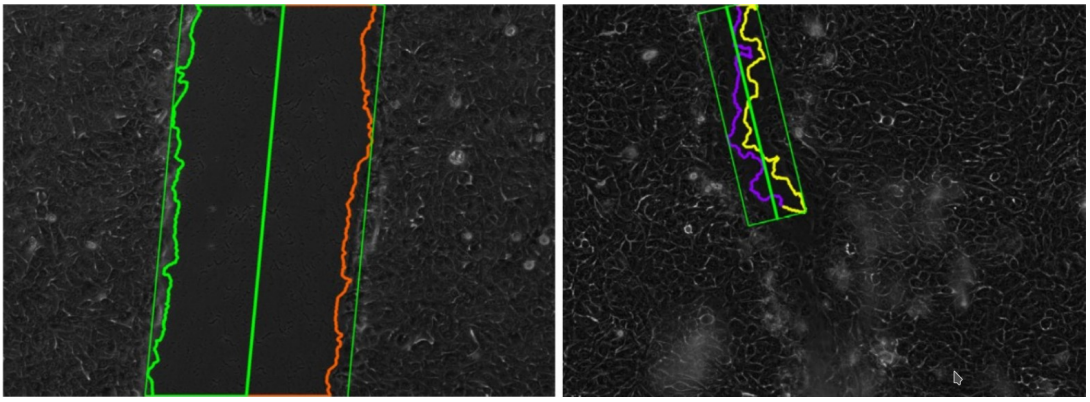

Figure 3.2.1.3.1. Images depicting the determination of the two wound front lines by the proposed algorithm on two frames corresponding to different timepoints.

The MSD (2) is calculated based on the extracted two wound fronts as depicted on the left part of the Figure 3.2.1.3.2. A graph of MSD-based wound front distance measures calculated across a complete wound healing assay (full time series data) are given in the right side of the Figure 3.2.1.3.2.

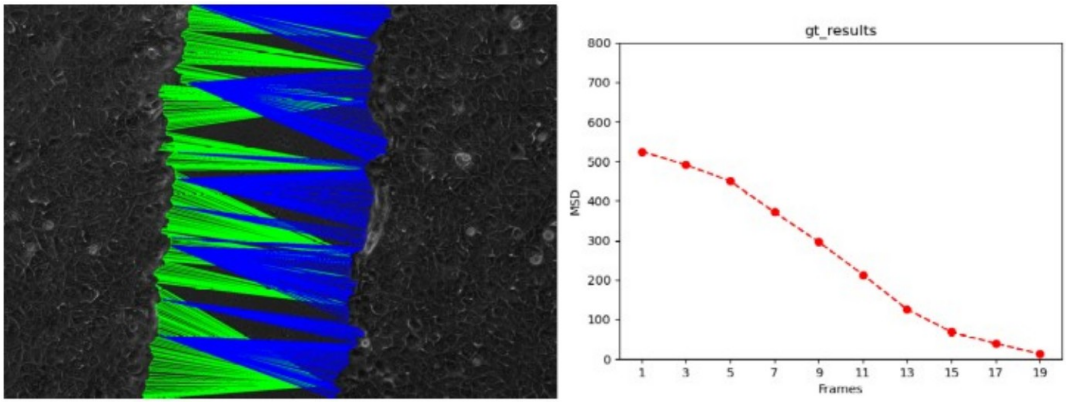

Figure 3.2.1.3.2. Left: Image for depicting the minimum cross distances used in Mean Surface Distance (MSD) calculation. **Right:** MSD-based wound front distance measures of a wound healing assay.

3.2.2. Data Generation

Studies for image synthesis, for applications such as data augmentation and realistic data generation, have recently made rapid progress with the breakthroughs of the Neural Style Transfer (NST) method and Generative Adversarial Networks (GANs). GAN-based methods have gained considerable attention for their ability to generate realistic and high-quality synthetic data by learning the underlying data distribution. While GANs have been used for both data augmentation and generation, the NST was not used for data generation tasks. On the other hand, the NST method has a simpler structure than GANs.

In this thesis, a novel NST-based approach for data generation alongside a novel method utilizing well established C-GAN-based approach are proposed and their synthesis capabilities for our specific problem are explored. Moreover, the performance of the NST method has been compared to that of a modified and fine-tuned conditional GAN (C-GAN). These methods have been applied to the conditional generation of phase-contrast microscopy wound healing assay time-series images. Binary segmentation maps representing the cell and wound regions are given as conditional inputs. Quantitative and qualitative results showed that our proposed NST-based data generation not only outperforms the modified C-GAN but also requires less resources. Furthermore, when utilized as a data augmentation method, it

has been demonstrated that the novel NST-based method improves segmentation performance.

3.2.2.1. Conditional GAN-Based Data Generation Method

To synthesize PCM images of wound healing assays, Isola et al.'s C-GAN model [26] is adopted as shown in Figure 3.2.2.1.1. The assay images were fed in as real inputs while the corresponding manually annotated segmentation masks served as the conditional inputs. We modified the architecture by replacing the L1-norm objective function with the mean of the Structural Dissimilarity Index Measure (DSSIM) and the L1-norm.

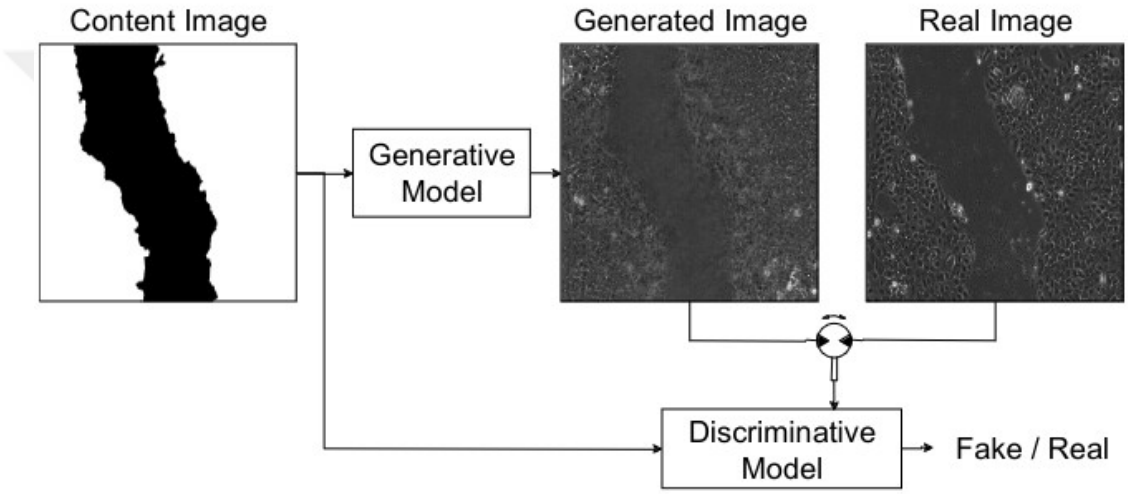

Figure 3.2.2.1.1. Overview of the C-GAN model developed for synthesizing phase-contrast microscopy images of wound healing assays.

The DSSIM measure was derived from the Structural Similarity Index Measure (SSIM) which computes the perceptual dissimilarity between two images by comparing their structural information [49]. The SSIM has previously been used as an additional loss term for training other GAN-based data generation methods [50]–[52]. The formulas of the SSIM and DSSIM are as given below:

$$SSIM(x,y) = \left(\frac{2\mu_x\mu_y + s_1}{\mu_x^2 + \mu_y^2 + s_1}\right)\left(\frac{2\sigma_{xy} + s_2}{\sigma_x^2 + \sigma_y^2 + s_2}\right),$$

$$DSSIM(x,y) = \frac{1 - SSIM(x,y)}{2}$$

DSSIM term is added as a supplementary loss function (SLF) together with L1-norm as the objective function of the C-GAN model to better preserve the structural features. The supplementary loss value is calculated by averaging the DSSIM and L1 loss values which are normalized between 0 and 1.

3.2.2.2. Neural Style Transfer Method

After the feed-forward NST method is proposed by Huang et al. as shown in Figure 3.2.2.2.1, style transfer became available without a separate training process for each input at inference. Additionally, the Adaptive Instance Normalization (AdaIN) layer aided the efficient transfer of feature statistics to the content input [32].

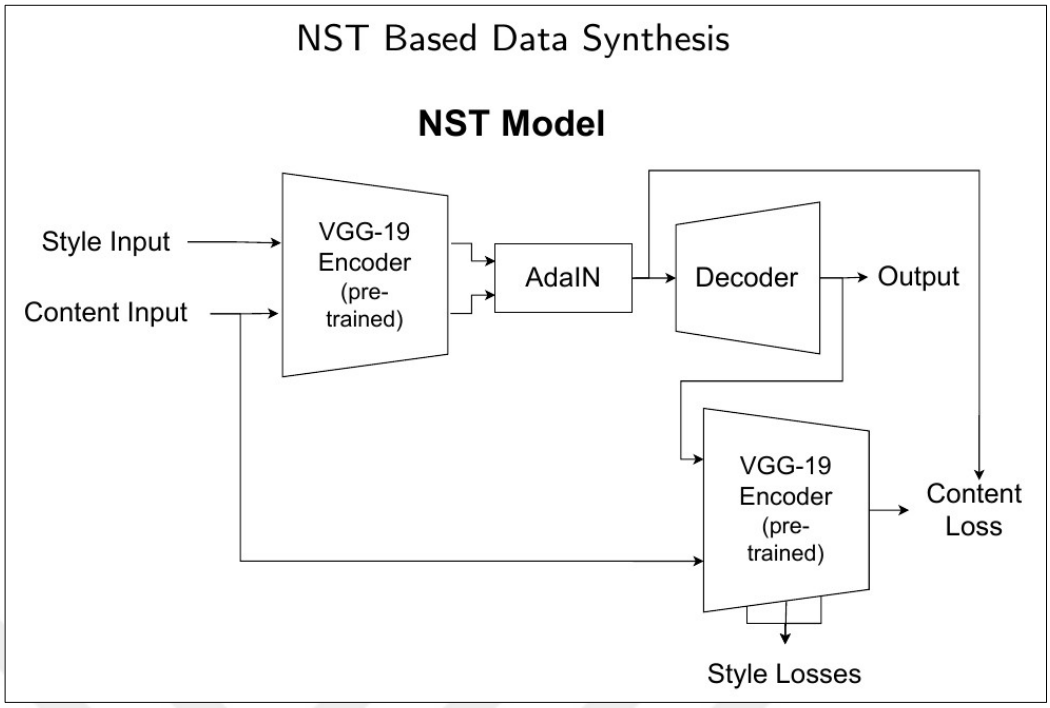

Figure 3.2.2.2.1. Overview of Huang et al.'s feed-forward neural style transfer model.

In this study, a novel high-resolution, low-cost data generation method is developed by utilizing NST for synthesizing phase-contrast microscopy wound healing assay data. The NST model takes a binary mask, which indicates the wound regions, as input. The content and style inputs were represented by the regions occupied by cell clusters and a real wound healing assay image respectively. Random noise was added directly to the content input. The outputs generated are high-resolution even under resource constraints thanks to patch-based training, the high-resolution inference process, and the simpler structure of the feed-forward NSTs as compared to GANs. Two separate models were trained for wound and cell regions to improve the quality of the results further.

3.2.2.2.1. Training Based on Patches

In the proposed method, while the feed-forward neural style transfer model was trained using patches of the image, during inference the trained model was used for generating the entire image at once as shown in Figure 3.2.2.2.1.1. In a similar manner, Huang et al. trained the NST model using smaller patches and obtained higher resolution outputs. We modified this approach to obtain even higher quality

results for synthetic data generation. In Huang et al.'s method, input images were first resized by making the shortest dimension 512 pixels and keeping the aspect ratio of the original input images same. Then, random patches of 256×256 pixel resolution were used in the training step and 512×512 pixel resolution images were generated at inference [32]. In this study, on the other hand, we maintained a high quality input, at a pixel resolution of 1920×1440 pixels, then patches of 512×512 pixels were used in the training phase. The resulting outputs were at 1920×1440-pixel resolution. The amount of memory required for inference was lower than that used in the training phase since there were no additional gradient calculations. This enabled processing of larger inputs at inference. It is worth noting that since the neural network model is fully convolutional, the input resolution may differ at training and inference times.

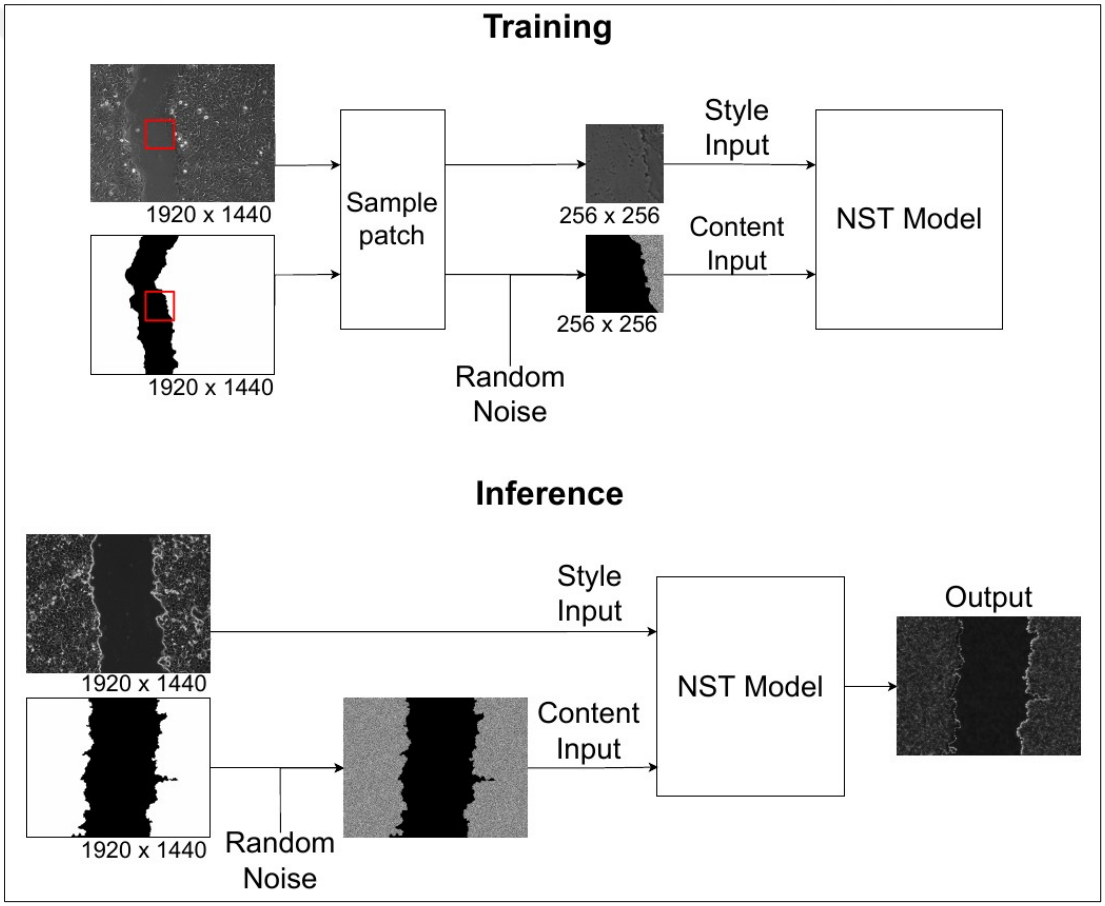

Figure 3.2.2.2.1.1. Overview of the patch-based style transfer method. The diagram above illustrates the patch training procedure. The diagram below shows the inference procedure yielding high resolution outputs via the trained model.

Processing the entire image at once at inference while training with patches enables achieving a higher accuracy despite limited memory. This approach concentrates the learning capability of the network to learn the visible local patterns within a patch at the cost of losing structural information at higher scales. Nevertheless, in images of cell groups there is not much structural pattern on a large-scale. Moreover, the integrity between patches is supplied by generating the image as a whole in the generation step. A visual comparison is given in Figure 3.2.2.2.1.2.

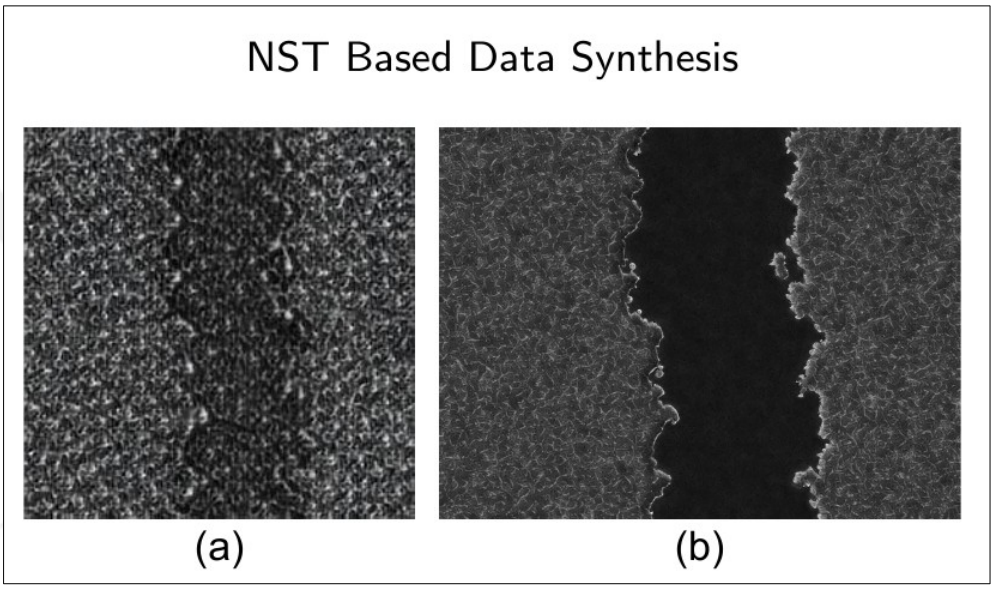

Figure 3.2.2.2.1.2. Visual comparison of with and without using patch-based training. (a) Synthesized image without using patch-based training. The output resolution is 512×512 pixels. (b) Synthesized image by using patch-based training and full resolution inference. The output resolution is 1920×1440 pixels.

3.2.2.2.2. Spatial Condition Input

Gatys et al. first introduced spatial control in NST [33]. Furthermore, Huang et al. utilized spatial control in a feed-forward NST model for the first time [32] by integrating a spatial control mask into the input. The spatial control mask is a binary image where the regions to be stylized are indicated with 1s, while 0s indicate regions that should not be affected. However, in the proposed method, rather than using a single model for style transfer with binary spatial control, two separate models were trained and used with binary content images of wound healing assays.

For generating the wound healing assay images, one model was trained to generate the empty regions (i.e. wound areas) while the second model was trained to generate regions occupied by cell clusters. The wound healing assay images could be generated by a single model as well. However, our experiments showed that using separate models to simplify the task improved the results. Furthermore, generating wound and cell regions separately allows using different style combinations, which improves the diversity of the results. The style inputs were masked using manual segmentation maps while training the respective models as shown in Figure 3.2.2.2.2.1.

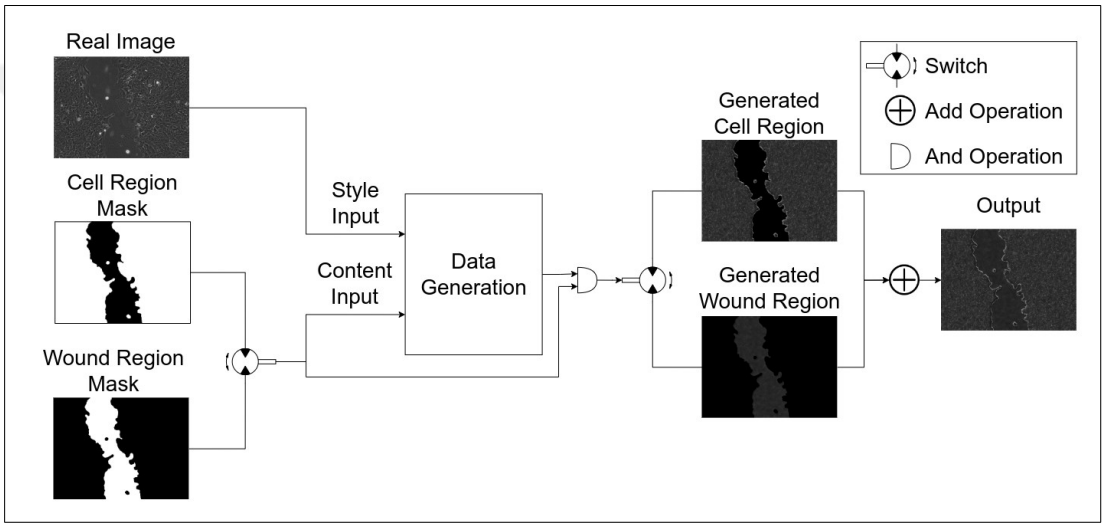

Figure 3.2.2.2.2.1. Diagram of the proposed NST-based data synthesis method with spatial control. The style input image is masked for wound and cell cluster regions separately. The segmentation mask is used for masking the wound regions and the inverse of the mask is used for masking the cell cluster regions. For generating the cell cluster regions or wound regions; respective style mask, target mask and model is used. After cell cluster regions and the wound regions are generated, they are combined to give the final output.

3.2.2.2.3. Noise Input

In contrast to Huang et al.'s method, and to increase the variations in the resulting wound healing assay images, random noise was added to the respective regions in the content image. Karras et al. utilized a similar idea for stochastic variation in data generation using GANs. Specifically, the authors input Gaussian noise at different layers of their network [31].

4. RESEARCH FINDINGS AND DISCUSSIONS

4.1. Semantic Segmentation Results

4.1.1. Traditional Approach Results

Figure 4.1.1. showcases performances of the classical methods for wound healing assay image segmentation utilizing dice coefficient score metric. The results show that the novel classical wound healing assay image segmentation method outperforms the existing methods in almost every frame and in the average Dice coefficient scores acquired from the two wound healing assay data from the test dataset.

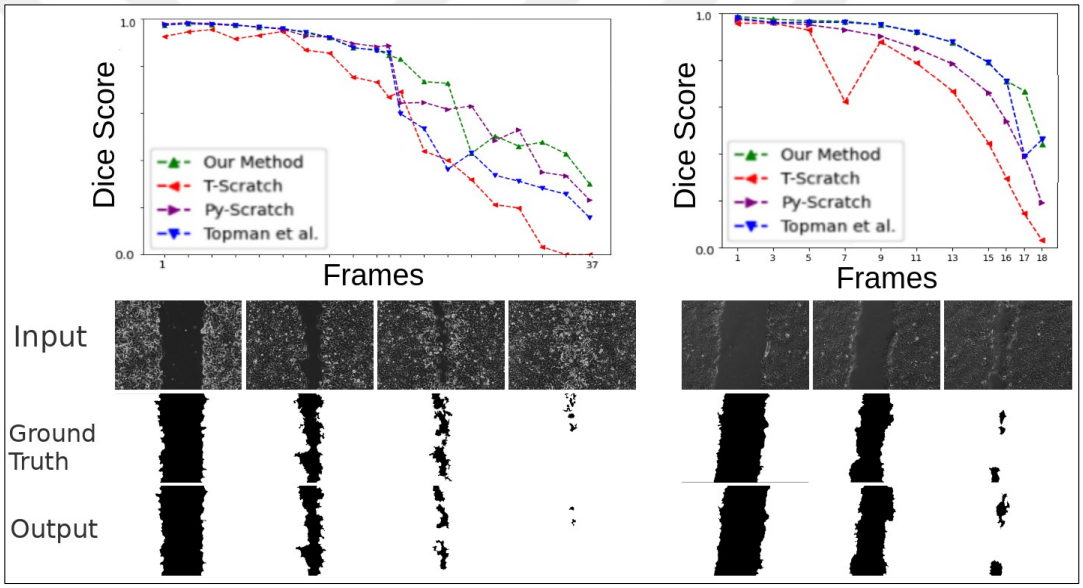

Figure 4.1.1. Figure of comparison between the classical wound healing assay segmentation methods and sample images from the applied test dataset. The graphs at the top include Dice coefficient scores of the classical segmentation methods. The images at the bottom illustrate original frames, ground truth segmentation masks and segmentation outputs of our classical segmentation method sampled throughout from two wound healing assays.

4.1.2. Deep-Learning Results

The Figure 4.1.2.1. shows exemplary results obtained by utilizing the standard U-Net and shallow U-Net models with 512×512 and 1024×1024 pixel resolutions. The obtained segmentation maps are overlayed with the ground truth maps where the gray-scale pixels show true positive cell regions, cyan pixels show true positive wound regions, yellow pixels show false positive wound regions, and magenta pixels show false positive cell regions.

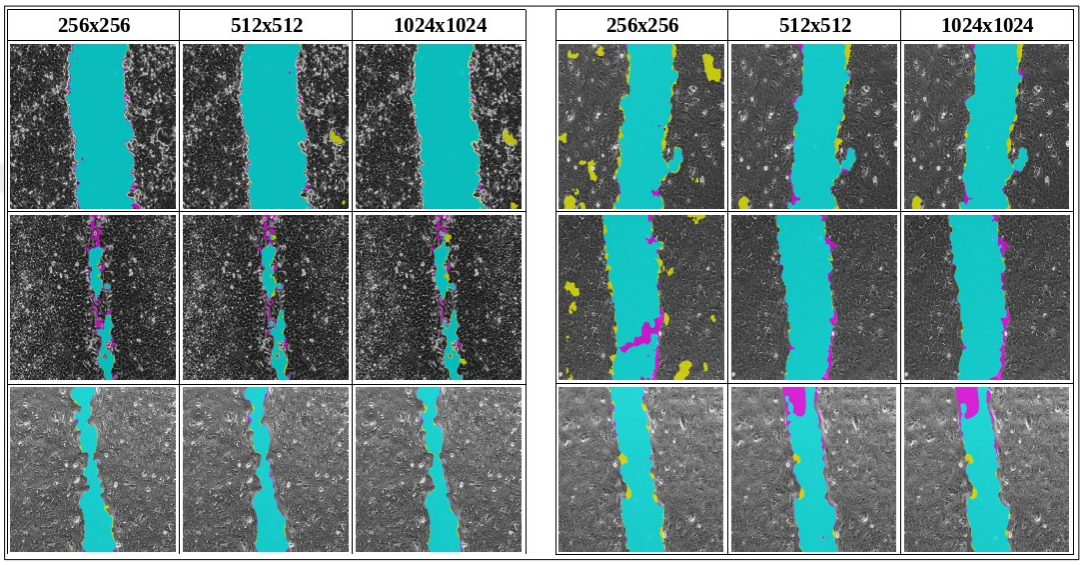

Figure 4.1.2.1. Sample results from the test dataset by the standard (left-most three columns) and shallow U-Net models. The segmentation maps obtained are overlayed with the ground truth maps, where grayscale pixels represent true positive cell regions, cyan pixels represent true positive wound regions, yellow pixels represent false positive wound regions, and magenta pixels represent false positive cell regions.

Table 4.1.2.1 presents quantitative comparison of shallow and high-resolution U-Net with standard U-Net models by surface-based and region-based metrics. These results depict that our proposed shallow U-Net with 1024×1024 pixel resolution achieves the best performance in both surface-based and region-based metrics.

Table 4.1.2.1. Quantitative comparison between standard U-Net model and shallow and high-resolution U-Net models using surface-based and region-based metrics on test dataset.

U-Net (256x256)		U-Net (512x512)		U-Net (1024x1024)	
Dice Score:	0.86 ± 0.14	**Dice Score:**	0.90 ± 0.16	**Dice Score:**	**0.91 ± 0.15**
Jaccard Ind.:	0.77 ± 0.17	**Jaccard Ind.:**	0.85 ± 0.18	**Jaccard Ind.:**	**0.85 ± 0.17**
MSD:	22.98 ± 31.57	**MSD:**	23.01 ± 100.43	**MSD:**	**13.03 ± 31.65**
HD:	179.09 ± 138.03	**HD:**	**110.71 ± 160.13**	**HD:**	119.58 ± 121.04
Avg. HD:	38.23 ± 42.80	**Avg. HD:**	40.35 ± 175.38	**Avg. HD:**	**22.52 ± 46.28**

Resizing operations are applied in the decoding side of the U-Net structure, after encoding part. Table 4.1.2.2. shows the impact of replacing these resizing layers with up convolution layers on wound healing segmentation problem.

Table 4.1.2.2. Comparison table between application of resizing and up-convolution operations in the U-Net based segmentation method by surface- and pixel-based metrics.

	Resize		Up-Convolution	
(256x256)U-Net	**Dice Score:**	**0.8577 ± 0.05**	**Dice Score:**	0.8345 ± 0.16
	Jaccard Ind.:	**0.7727 ± 0.07**	**Jaccard Ind.:**	0.7398 ± 0.18
	MSD:	**10.5893 ± 5.13**	**MSD:**	**10.6325 ± 16.59**
	HD:	**75.7822 ± 36.11**	**HD:**	74.8773 ± 62.16
	Avg. HD:	**17.8874 ± 7.93**	**Avg. HD:**	**17.8490 ± 19.58**
	Resize		**Up-Convolution**	
U-Net (512x512)	**Dice Score:**	**0.9327 ± 0.02**	**Dice Score:**	0.8838 ± 0.17
	Jaccard Ind.:	**0.8860 ± 0.03**	**Jaccard Ind.:**	0.8208 ± 0.19
	MSD:	**3.9466 ± 1.81**	**MSD:**	10.7581 ± 42.61
	HD:	**33.8289 ± 10.03**	**HD:**	58.0324 ± 78.47
	Avg. HD:	**6.8967 ± 2.57**	**Avg. HD:**	18.6283 ± 74.09

Results in the Table 4.1.2.2. show that there is no significant improvement obtained by replacing the resize operations with up-convolution operations during

the decoding phase in the U-Net model. Furthermore, up-convolution layer requires more computational resource as compared to the resizing operation.

4.2. Data Generation Results

4.2.1. Quantitative Evaluation Metrics

In this study, SSIM, Multiscale structural similarity (MS-SSIM), and Peak Signal-to-Noise Ratio (PSNR) metrics were used for quantitative assessment of image synthesis via ablation studies, and Fréchet inception distance (FID) [53] metric was used for more delicate quality comparison of the generated images which aims to quantify how humans perceive the quality of a given set of images.

MS-SSIM is a multi-scaled version of the SSIM metric, where the SSIM is calculated for the image at different resolutions. In this paper, the original image was half-sampled 4 times, the SSIM was calculated for each resolution, and the average is reported.

PSNR is a well-known metric used for measuring the quality of images in many image-processing applications when there is a ground-truth image to be compared. It is computed as shown below:

$$MAX = 255,$$

$$MSE = \frac{1}{width \times height} \sum_{x=1}^{width} \sum_{y=1}^{height} (Y_{(x,y)} - \hat{Y}_{(x,y)})^2,$$

$$PSNR = 10 \times log_{10} \left(\frac{MAX^2}{MSE} \right)$$

where Y and $\hat{Y}$ denote the true and generated images, respectively.

To quantify the perceived quality of the generated images, the FID was used. The FID metric, which was initially developed for real object images, has also been used to assess medical data [54], [55]. It was developed to compare distances of "perceptual" distributions between two datasets. To calculate the perceptual distance, high level semantic feature maps are generated by a pre-trained Inception neural network model.

The Inception-V3 model used as feature extractor for FID was originally trained with images of size 299×299 pixels [56]. However, since the Inception model is a fully convolutional neural network, the FID score can be calculated for images with different resolutions. In our study, the FID score was calculated for high resolution images since one advantage of the NST-based data generation method is its high-resolution output. However, FID score for standard resolution is also calculated according to convention. Bicubic interpolation was used in the resizing operation. The FID metric is calculated by down-scaling images to 299×299-pixel resolution unless a different resolution is explicitly denoted in this paper.

4.2.2. Ablation Studies

The performance metrics presented in ablation studies were calculated on the test set. The entire wound healing dataset was randomly partitioned into 80% for training and 20% for testing.

We tested the effect of DSSIM loss term on the performance of the C-GAN. The PSNRs of the generated results to the ground truth images were used to compare the L1 and L1-DSSIM supplementary loss functions (SLFs).

Table 4.2.2.1 shows average PSNR values calculated over 44 test frames of 2 different assays from our dataset. Figure 4.2.2.1 also shows sample synthesized images with the corresponding PSNR values of the generated images comparing L1 and L1-DSSIM SLFs in the C-GAN's objective function.

Table 4.2.2.1. Average PSNR values derived from generated images from the C-GAN models trained by using L1 and L1-DSSIM supplementary loss functions (SLFs) separately. 44 images were generated by using mask images from our test-set. Each model is trained for 1000 epochs.

	SLF (L1)	SLF (L1 - DSSIM)
Average PSNR:	8.97 ± 0.13	9.18 ± 0.11

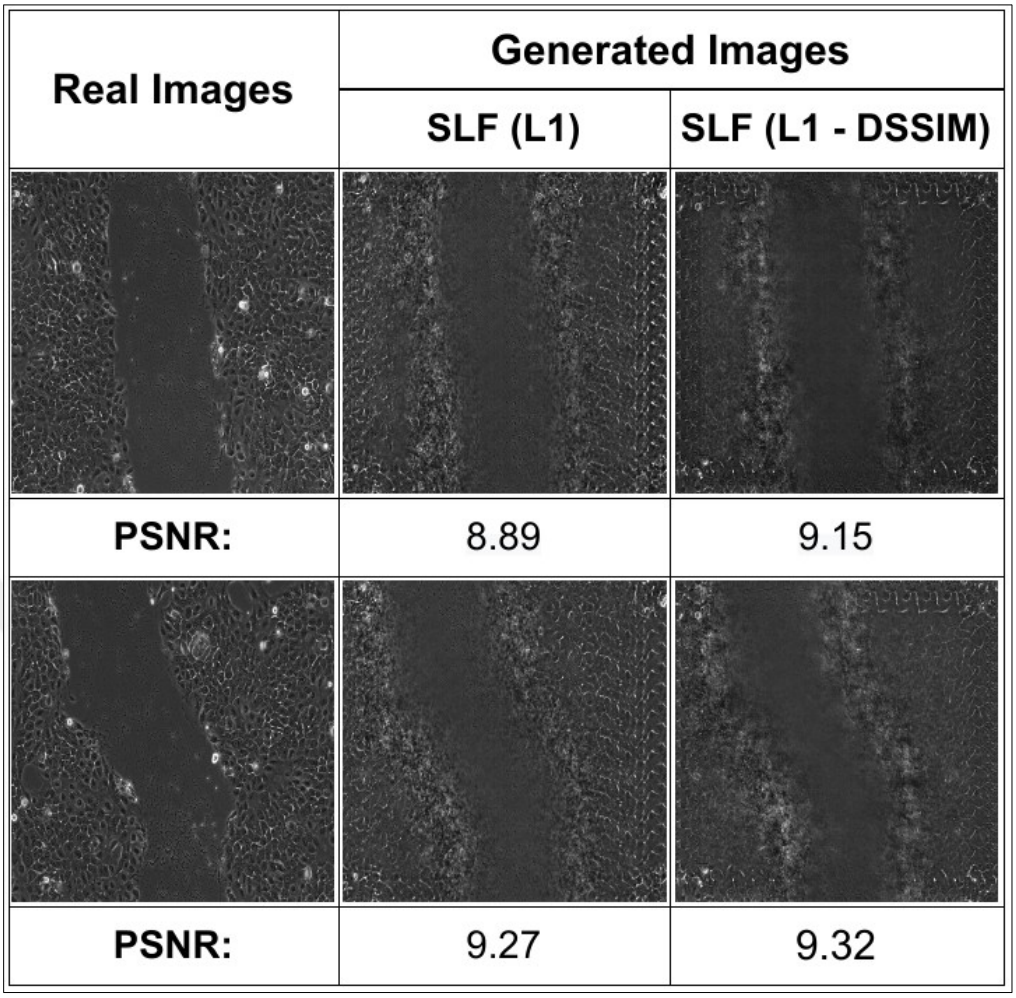

Figure 4.2.2.1. Comparison between L1 and L1-DSSIM supplementary loss functions (SLFs) used in C-GAN model training. Each model is trained for 1000 epochs.

The average PSNR values in Table 4.2.2.1 and the sample synthesized images in Figure 4.2.2.1 show that, using average of L1 and DSSIM as the SLF improves realistic details and reduces visible repetitive artifacts. The increase in the PSNR values supports that using DSSIM together with the L1 distance loss function results in better synthesis.

Table 4.2.2.2 shows the performance comparison of synthesizing wound healing assay images with the proposed NST-based method by using a single model

for the whole image vs. two separate models for cell cluster and empty wound regions via the SSIM, MS-SSIM, and PSNR metrics.

Table 4.2.2.2. Comparison of single and multiple models for generating the cell cluster and the empty wound regions

Method	SSIM↑	MS-SSIM↑	PSNR↑
Single Model	0.3332	0.2831	7.3542
Separate Models	**0.3804**	**0.3309**	**7.4190**

Table 4.2.2.3 presents the FID metric performance comparison of patch-based and down-sampled images as training inputs of the NST model. As observed, patch-based approach yields lower FID scores and thus outperforms the down-sampling based approach.

Table 4.2.2.3. FID metric comparison of patch-based training and training with down-sampled inputs.

Method	FID↓
Down-Sampling	347.0227
Patch-Based	**340.0559**

4.2.3. Quantitative Evaluation Results

The images in Figure 4.2.3.1. show sample results, input masks and the real images that the mask is produced from. Each row pair displays the real images and corresponding masks of the consecutive frames from the same assays. As it can be deduced visually, the images generated by the C-GAN based method have similar artifacts and similar styles in every sample, even though the input masks are different. On the contrary, the images generated by the proposed NST-based method do not produce repetitive artifacts; they depict large variations in cell-shapes and

distributions, even when the input masks are similar. Furthermore, the styles of the overall images are more diverse compared to the results of the C-GAN method.

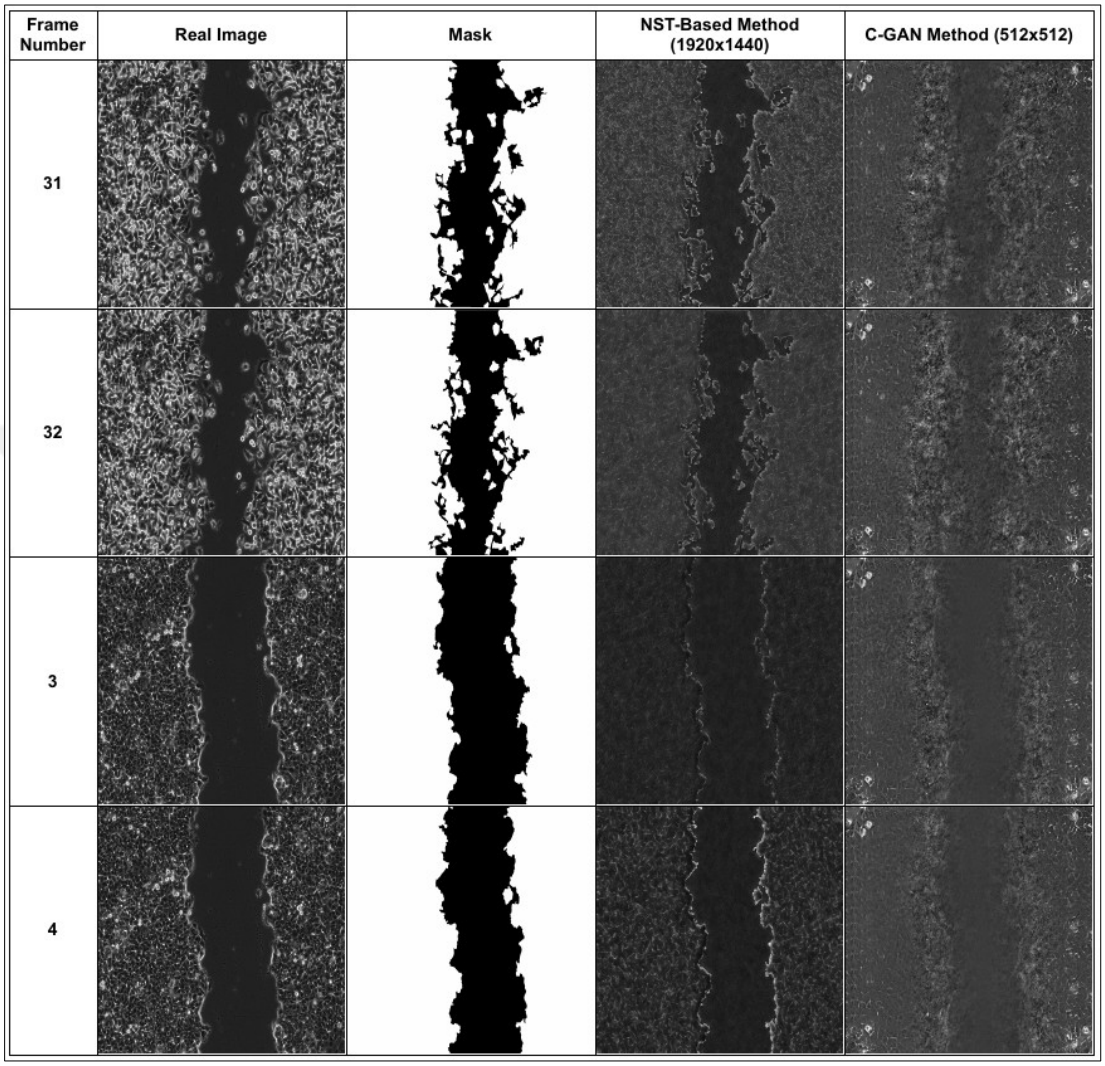

Figure 4.2.3.1. Samples of synthesized phase-contrast wound healing assay images generated by both the proposed NST-based method and the C-GAN method. The first two columns display the original images along with their corresponding masks, while the third and fourth columns display the images generated by our proposed method and the C-GAN method, respectively.

The results in Table 4.2.3.1. provide the perceptual quality comparison between our NST-based method and the C-GAN method. The FID values are calculated for 299×299 and 1920×1440 pixel resolutions. It is worth noting that even

though the C-GAN based method was trained to generate lower resolution outputs (512×512), the FID scores calculated on lower resolution are better for our NST-based method, which has outputs at 1920×1440 pixel resolution.

Table 4.2.3.1. Comparison of the FID metric using 5-fold cross-validation is conducted between our novel NST-based method and the C-GAN method for the generation of wound healing assay data.

Fold Index	Proposed NST Method		C-GAN Method	
	FID↓ (299x299)	FID↓ (1920x1440)	FID↓ (299x299)	FID↓ (1920x1440)
1	367.53	37.33	523.51	48.87
2	568.43	48.32	453.52	49.03
3	487.43	40.99	388.20	41.90
4	336.04	35.29	359.44	47.43
5	395.50	43.73	428.29	55.95
Avg.:	**410.92**	**41.43**	430.59	48.64

4.2.4. Qualitative Evaluation Results

In addition to comparison by quantitative metrics, we compared the image synthesis performances of the methods by subjective evaluation of the domain experts as shown in Figure 4.2.4.1.

We took two frames each from the 14 assays in our dataset for qualitative evaluation by domain experts. The two frames, along with their manual annotations, were taken from the beginning and end of the assays to enrich the diversity in the collected frames. Manual annotations were input as conditions to synthesize wound healing assay images by the C-GAN and NST methods. The models that were used to generate the synthesized data were trained on the portion of the ground-truth data excluding the assays that include the binary maps that were in the input set as in the k-fold cross validation.

A total of 7 molecular biologists who worked on the phase-contrast microscopy wound healing data before were individually invited to rate the 28 synthesized data

by their naturalism and artifact-freeness, separately. The observers are categorized as "novices" and "experts" based on their practical experience on working with (i.e. acquiring and analyzing) similar data. 2 observers were considered as "experts" (>6 months of experience) while the remaining 5 were "novices" (1-6 months of experience). The naturalism attribute was rated between 1 and 5, where 1 corresponds to “not realistic” and 5 corresponds to “very realistic (indistinguishable)”. The artifact-freeness attribute was also rated between 1 and 5, where 1 corresponds to “contains many artifacts” and 5 corresponds to “no artifacts”. For a reference, the condition input and the corresponding real image were also shown to the participants together with the synthesized data. The synthesized data was shown to the subjects by hiding the source and the order of the data was randomly shuffled to prevent any bias.

	Naturalism		Artifact-Freeness	
	NST-Based (Ours)	**GAN-Based**	**NST-Based (Ours)**	**GAN-Based**
	Experts			
Average:	**3.25 ± 0.31**	2.30 ± 0.37	**3.81 ± 0.29**	1.79 ± 0.22
	Novices			
Average:	**2.27 ± 0.11**	1.79 ± 0.18	**3.77 ± 0.64**	1.84 ± 0.14
	Overall			
Average:	**2.97 ± 0.35**	2.15 ± 0.34	**3.80 ± 0.36**	1.80 ± 0.19

(a)

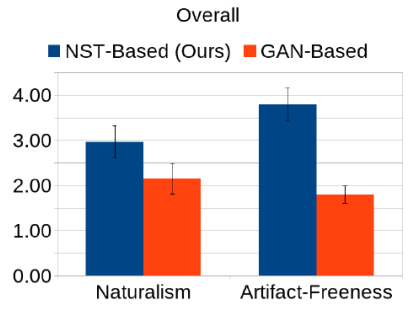

(b)

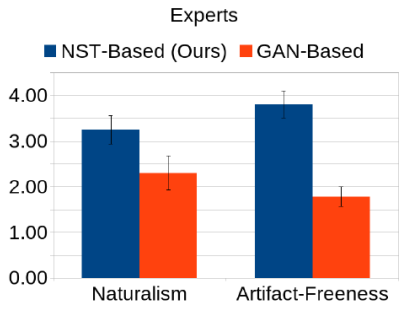

(c)

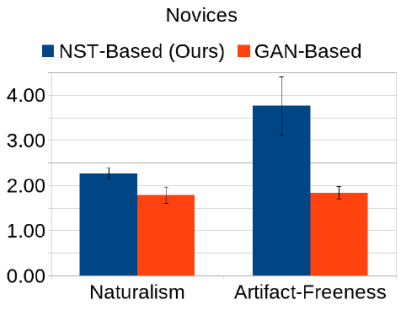

(d)

Figure 4.2.4.1. Results of qualitative assessment for the naturalism and artifact-freeness attributes of synthesized images by NST-based and GAN-based methods. (a) Numeric results of quantitative assessment by novices and experts; (b) overall scores; (c) scores by expert observers; (d) scores by novice observers.

The results in Figure 4.2.4.1. indicate that the NST-based data generation method outperforms the C-GAN method in synthesizing more realistic and more artifact-free wound healing assay images with a high margin according to professionals' perception. While our method is favored in both attributes including naturalism, it is favored by a higher margin for artifact-freeness.

The impact of including the generated images, by the novel NST-based method, in the training data of a semantic segmentation task is demonstrated. Accordingly, a modified U-Net [29] model is trained to segment the wound front in wound healing assays. The modification to the U-net architecture mitigates the trade-off between training with high-resolution images and the availability of training resources. Briefly, the size of the feature maps is increased, and then, to balance the amount of memory used, the number of the generated feature maps is decreased. The convolutional layers are reduced to decrease the number of the feature maps. By this way, the inputs and outputs of the segmentation model were increased to 512×512 from 256×256 pixel resolution.

From the 328 images in the wound healing assay time-series image dataset, 79 images were separated for testing. The remaining 249 images belonging to 12 wound healing assays were used for training of the data augmentation models and the segmentation model. Figure 4.2.4.2. shows the performance metrics of the modified U-Net segmentation models that were trained on different sets of data.

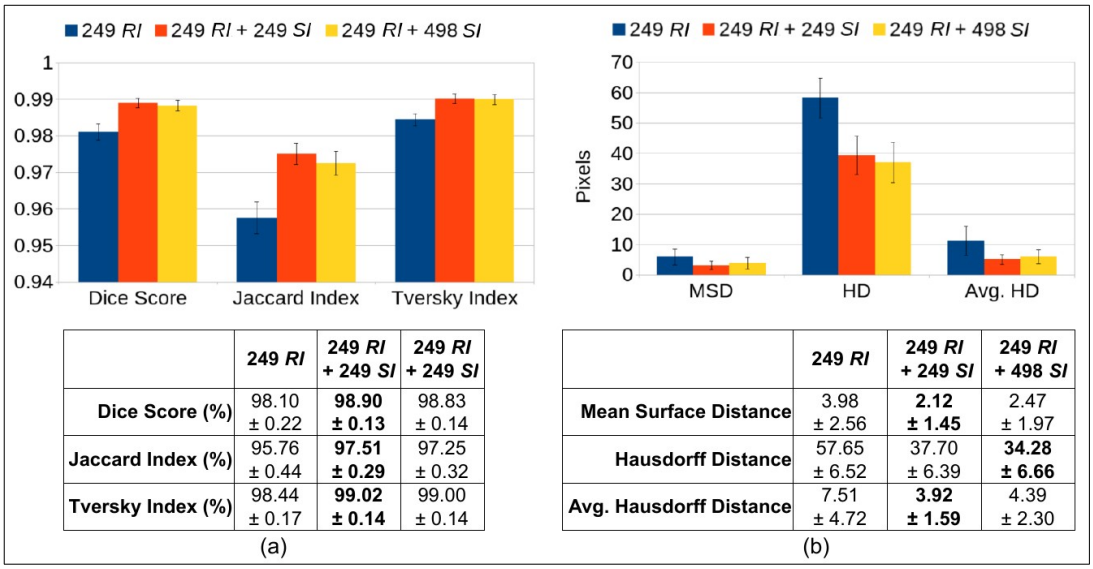

	249 *RI*	249 *RI* + 249 *SI*	249 *RI* + 249 *SI*
Dice Score (%)	98.10 ± 0.22	**98.90 ± 0.13**	98.83 ± 0.14
Jaccard Index (%)	95.76 ± 0.44	**97.51 ± 0.29**	97.25 ± 0.32
Tversky Index (%)	98.44 ± 0.17	**99.02 ± 0.14**	99.00 ± 0.14

(a)

	249 *RI*	249 *RI* + 249 *SI*	249 *RI* + 498 *SI*
Mean Surface Distance	3.98 ± 2.56	**2.12 ± 1.45**	2.47 ± 1.97
Hausdorff Distance	57.65 ± 6.52	37.70 ± 6.39	**34.28 ± 6.66**
Avg. Hausdorff Distance	7.51 ± 4.72	**3.92 ± 1.59**	4.39 ± 2.30

(b)

Figure 4.2.4.2. Validation results of segmentation by the U-Net based model that is trained using different sets of data with a confidence interval of 95%. The U-Net model is trained with 249 real training data until overfitting and the best performing model according to the validation loss value is resulted. The same procedure is repeated two times on the last trained model by adding 249 synthesized data using the NST-based method. RI stands for real images, while SI stands for synthetic images. (a) Set similarity metrics; (b) surface distance-based metrics.

The results shown in Figure 4.2.4.2. were obtained from the modified U-Net models that are taken from 3 stages of the training process with different datasets. At the first stage 249 real data used as the training data. In the next 2 stages, 249 synthesized images, by our NST-based method, are added to the training set. The training is performed for 200 epochs in each stage. For each new stage, the best performing model from the last stage is taken for training. The NST-based model used for generating these 249 data is trained by using only the data from training set. Figure 4.2.2.3. shows the binary cross entropy loss values during these training steps.

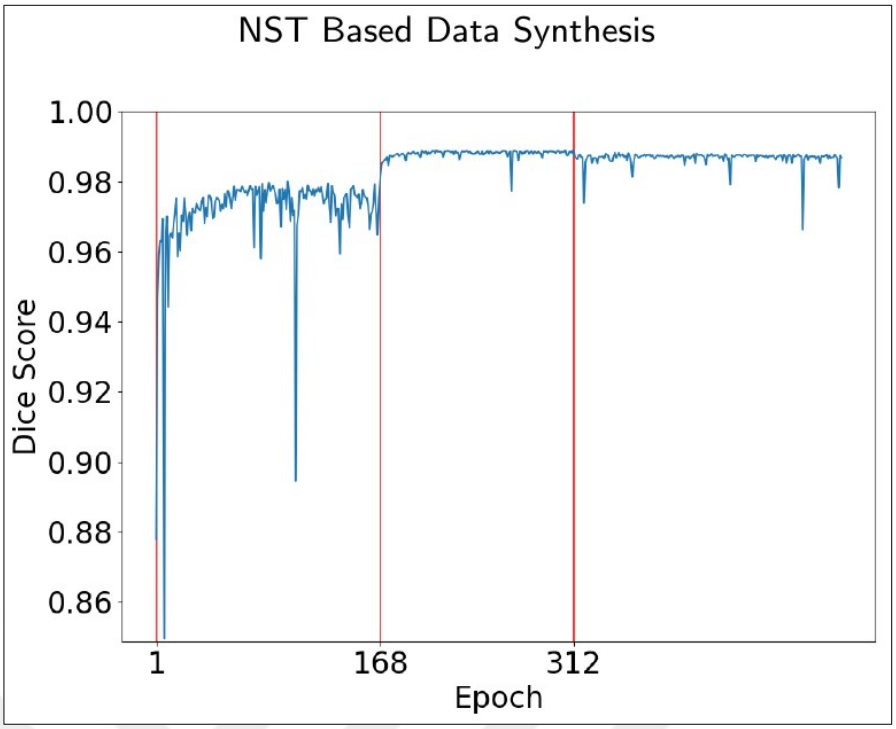

Figure 4.2.4.3. The graph of validation Dice scores from the training of the modified U-Net segmentation model per epoch. The training has 3 stages composed of 200 epochs each. In the first stage, 249 real data were used in the training. For the next stages, 249 newly generated images by our NST-based method were added to the training dataset. Except for the last stage, validation scores after the best-performed epochs are not included in the graph. These epochs are marked by red lines.

According to the results in Figure 4.2.4.3. the wound healing assay data synthesized by our NST-based method contributed to the segmentation performance as training data. The validation scores of the segmentation model increased from 98.11% to 98.93% in Dice score and in Jaccard index increased from 95.76% to 97.56% with 95% confidence interval by using 249 synthesized images in addition to the initial dataset consisting of 249 real data. Doubling the number of synthesized images and continuing the training did not contribute to segmentation performance any further.

5. CONCLUSIONS, CONTRIBUTIONS AND FUTURE WORK

Our proposed traditional computer vision-based method for segmenting wound fronts in wound healing assays, utilizes variance filtering, Gaussian smoothing, dilation, and erosion operations to achieve accurate segmentation results. By considering temporal information and the characteristic shrinkage of wound regions over time, the method effectively identifies and assigns potential wound regions. This approach provides a valuable tool for automated and reliable wound front segmentation in wound healing assays, contributing to the advancement of wound healing research.

The examined traditional method requires Gaussian blurring kernel parameter to be fine-tuned for segmentation which corresponds to the approximate pixel value of the radius of the cells in the assay images. In the future a prepossessing method can be applied for estimating the value of this kernel parameter automatically to provide a fully-automated solution.

U-Net based segmentation is also an automated method with higher accuracy when there is efficient amount of training data and computational power. Application of shallow and high-resolution U-Net based method increases the performance by requiring same amount of computational resource as compared to the standard U-Net model.

In this study, also a novel Neural Style Transfer (NST) based data generation method for generating phase-contrast microscopy data of wound healing assays is examined. It is concluded that the NST-based method performs better than Conditional Generative Adversarial Network (C-GAN) under constraints of computational resources. The qualitative and quantitative metrics show that our proposed patch-based NST-based method outperforms the C-GAN alternative in terms of quality and diversity of the generated images.

To the best of our knowledge, this is the first NST-based method proposed for data generation task which does not use GAN. While we demonstrated the NST-based method for synthesizing phase-contrast microscopy (PCM) time-lapse images

of wound healing assays, this approach is the first of its kind for any type of imagery as far as we know. NST-based data generation method by not using GAN is less resource demanding and easier to train since the latter one has adversarial training procedure. Our NST-based method's inference time is ~3.3 seconds while C-GAN method's is only ~33 milliseconds. On the other hand, training of the NST-based method takes only ~2.5 minutes while training the C-GAN based method takes ~25 hours.

Also, as far as we know, this is the first synthesis method proposed for generating artificial wound healing assay data that does not require any additional calculation of (thus prior information on) cell distribution statistics. The model learns the cell distribution from the input data and with the style input and random noise input, the cells are distributed. Our NST-based data generation method theoretically can generate infinitely many different results by changing the input conditions and/or the noise input. Even though the cell distribution is generated automatically, wound region mask input is required for controlling cell and wound regions in our algorithm. The code for generating the results will be available at http://https://github.com/IDU-CVLab/NST_for_Gen upon appropriate request. In future work, the condition mask can be automatically generated to increase variability.

In future work, AdaIN can be used in many layers to better preserve structural information, yet this approach may require more computational resources. Also, the noise input can be applied in multiple layers instead of a single layer for improving the diversity in the generated images.

REFERENCES

[1] J. E. N. Jonkman *et al.*, "An introduction to the wound healing assay using live-cell microscopy," *Cell Adhesion and Migration*. 2014, doi: 10.4161/cam.36224.

[2] J. Pijuan *et al.*, "In vitro cell migration, invasion, and adhesion assays: From cell imaging to data analysis," *Front. Cell Dev. Biol.*, 2019, doi: 10.3389/fcell.2019.00107.

[3] E. C. Jensen, "Use of Fluorescent Probes: Their Effect on Cell Biology and Limitations," *Anatomical Record*. 2012, doi: 10.1002/ar.22602.

[4] F. Progatzky, M. J. Dallman, and C. Lo Celso, "From seeing to believing: Labelling strategies for in vivo cell-tracking experiments," *Interface Focus*. 2013, doi: 10.1098/rsfs.2013.0001.

[5] F. Milde, D. Franco, A. Ferrari, V. Kurtcuoglu, D. Poulikakos, and P. Koumoutsakos, "Cell Image Velocimetry (CIV): Boosting the automated quantification of cell migration in wound healing assays," *Integr. Biol. (United Kingdom)*, 2012, doi: 10.1039/c2ib20113e.

[6] K. Eliceiri, C. A. Schneider, W. S. Rasband, and K. W. Eliceiri, "NIH Image to ImageJ : 25 years of image analysis HISTORICAL commentary NIH Image to ImageJ : 25 years of image analysis," *Nat. Methods*, 2012, doi: 10.1038/nmeth.2089.

[7] T. Gebäck, M. M. P. Schulz, P. Koumoutsakos, and M. Detmar, "TScratch: A novel and simple software tool for automated analysis of monolayer wound healing assays," *Biotechniques*, 2009, doi: 10.2144/000113083.

[8] Y. Matsubayashi, W. Razzell, and P. Martin, "'White wave' analysis of epithelial scratch wound healing reveals how cells mobilise back from the leading edge in a myosin-II-dependent fashion," *J. Cell Sci.*, 2011, doi: 10.1242/jcs.080853.

[9] M. D. Zordan, C. P. Mill, D. J. Riese, and J. F. Leary, "A high throughput, interactive imaging, bright-field wound healing assay," *Cytom. Part A*, 2011, doi: 10.1002/cyto.a.21029.

[10] A. Suarez-Arnedo, F. T. Figueroa, C. Clavijo, P. Arbeláez, J. C. Cruz, and C. Muñoz-Camargo, "An image J plugin for the high throughput image analysis of in vitro scratch wound healing assays," *PLoS One*, 2020, doi: 10.1371/journal.pone.0232565.

[11] G. Topman, O. Sharabani-Yosef, and A. Gefen, "A standardized objective method for continuously measuring the kinematics of cultures covering a mechanically damaged site," *Med. Eng. Phys.*, 2012, doi: 10.1016/j.medengphy.2011.07.014.

[12] T. C. Wang *et al.*, “Video-to-video synthesis,” 2018.

[13] Y. Wang, C. Wang, and Z. Zhang, “Segmentation of clustered cells in negative phase contrast images with integrated light intensity and cell shape information,” *J. Microsc.*, 2018, doi: 10.1111/jmi.12673.

[14] S. Mahmud *et al.*, “A Shallow U-Net Architecture for Reliably Predicting Blood Pressure (BP) from Photoplethysmogram (PPG) and Electrocardiogram (ECG) Signals,” *Sensors*, 2022, doi: 10.3390/s22030919.

[15] A. Vaswani *et al.*, “Attention is all you need,” 2017.

[16] O. Oktay *et al.*, “Attention u-net: Learning where to look for the pancreas,” 2018.

[17] B. Mayalive, O. Saylig, Ö. Y. Özuysal, D. P. Okvur, B. U. Töreyin, and D. Ünay, “Automated Analysis of Wound Healing Microscopy Image Series - A Preliminary Study,” 2020, doi: 10.1109/TIPTEKNO50054.2020.9299213.

[18] A. Javer, J. Rittscher, and H. Z. Sailem, “DeepScratch: Single-cell based topological metrics of scratch wound assays,” *Comput. Struct. Biotechnol. J.*, 2020, doi: 10.1016/j.csbj.2020.08.018.

[19] J. Oldenburg *et al.*, “Methodology for comprehensive cell-level analysis of wound healing experiments using deep learning in MATLAB,” *BMC Mol. Cell Biol.*, 2021, doi: 10.1186/s12860-021-00369-3.

[20] P. Sermanet, D. Eigen, X. Zhang, M. Mathieu, R. Fergus, and Y. LeCun, “Overfeat: Integrated recognition, localization and detection using convolutional networks,” 2014.

[21] H. Kaiming, Z. Xiangyu, R. Shaoqing, and S. Jian, “Delving Deep into Rectifiers: Surpassing Human-Level Performance on ImageNet Classification Kaiming,” *Biochem. Biophys. Res. Commun.*, 2018.

[22] A. Prasoon, K. Petersen, C. Igel, F. Lauze, E. Dam, and M. Nielsen, “Deep feature learning for knee cartilage segmentation using a triplanar convolutional neural network,” 2013, doi: 10.1007/978-3-642-40763-5_31.

[23] F. Liu, C. Shen, G. Lin, and I. Reid, “Learning Depth from Single Monocular Images Using Deep Convolutional Neural Fields,” *IEEE Trans. Pattern Anal. Mach. Intell.*, 2016, doi: 10.1109/TPAMI.2015.2505283.

[24] M. Frid-Adar, I. Diamant, E. Klang, M. Amitai, J. Goldberger, and H. Greenspan, “GAN-based synthetic medical image augmentation for increased CNN performance in liver lesion classification,” *Neurocomputing*, 2018, doi: 10.1016/j.neucom.2018.09.013.

[25] T. Salimans, I. Goodfellow, W. Zaremba, V. Cheung, A. Radford, and X. Chen, “Improved techniques for training GANs,” 2016.

[26] P. Isola, J. Y. Zhu, T. Zhou, and A. A. Efros, “Image-to-image translation with conditional adversarial networks,” 2017, doi: 10.1109/CVPR.2017.632.

[27] J. Y. Zhu *et al.*, “Toward multimodal image-to-image translation,” 2017.

[28] I. J. Goodfellow *et al.*, “Generative adversarial nets,” 2014, doi: 10.1007/978-3-658-40442-0_9.

[29] O. Ronneberger, P. Fischer, and T. Brox, “U-Net: Convolutional Networks for Biomedical Image Segmentation [2015; First paper exploring U-Net architecture.],” 2015.

[30] C. Li and M. Wand, “Precomputed real-time texture synthesis with markovian generative adversarial networks,” 2016, doi: 10.1007/978-3-319-46487-9_43.

[31] T. Karras, S. Laine, and T. Aila, “A Style-Based Generator Architecture for Generative Adversarial Networks,” *IEEE Trans. Pattern Anal. Mach. Intell.*, 2019, doi: 10.1109/TPAMI.2020.2970919.

[32] X. Huang and S. Belongie, “Arbitrary Style Transfer in Real-Time with Adaptive Instance Normalization,” 2017, doi: 10.1109/ICCV.2017.167.

[33] L. A. Gatys, A. S. Ecker, and M. Bethge, “Image Style Transfer Using Convolutional Neural Networks,” 2016, doi: 10.1109/CVPR.2016.265.

[34] A. Atapour-Abarghouei and T. P. Breckon, “Real-Time Monocular Depth Estimation Using Synthetic Data with Domain Adaptation via Image Style Transfer,” 2018, doi: 10.1109/CVPR.2018.00296.

[35] M. Gu, S. Vesal, R. Kosti, and A. Maier, “Few-shot Unsupervised Domain Adaptation for Multi-modal Cardiac Image Segmentation,” 2022, doi: 10.1007/978-3-658-36932-3_5.

[36] R. Yamashita, J. Long, S. Banda, J. Shen, and D. L. Rubin, “Learning Domain-Agnostic Visual Representation for Computational Pathology Using Medically-Irrelevant Style Transfer Augmentation,” *IEEE Trans. Med. Imaging*, 2021, doi: 10.1109/TMI.2021.3101985.

[37] P. A. Cicalese, A. Mobiny, P. Yuan, J. Becker, C. Mohan, and H. Van Nguyen, “StyPath: Style-Transfer Data Augmentation for Robust Histology Image Classification,” 2020, doi: 10.1007/978-3-030-59722-1_34.

[38] X. Zheng, T. Chalasani, K. Ghosal, S. Lutz, and A. Smolic, “Stada: Style transfer as data augmentation,” 2019, doi: 10.5220/0007353401070114.

[39] J. Philip T., A.-A. Amir, B. Stephen, B. Toby P., and O. Boguslaw, “Style Augmentation: Data Augmentation via Style Randomization,” 2019.

[40] A. Mikolajczyk and M. Grochowski, “Style transfer-based image synthesis as an efficient regularization technique in deep learning,” 2019, doi: 10.1109/MMAR.2019.8864616.

[41] R. Theagarajan and B. Bhanu, “DeepHesc 2.0: Deep generative multi adversarial networks for improving the classification of hESC,” *PLoS One*, vol. 14, no. 3, 2019, doi: 10.1371/journal.pone.0212849.

[42] O. Bailo, D. Ham, and Y. M. Shin, “Red blood cell image generation for data augmentation using conditional generative adversarial networks,” 2019, doi: 10.1109/CVPRW.2019.00136.

[43] Ting-Chun Wang, M.-Y. Liu, Jun-Yan Zhu, Andrew Tao, Jan Kautz, and Bryan Catanzaro, “High-Resolution Image Synthesis and Semantic Manipulation with Conditional GANs Ting-Chun,” *Proc. IEEE Comput. Soc. Conf. Comput. Vis. Pattern Recognit.*, 2018.

[44] C. Fu *et al.*, “Three dimensional fluorescence microscopy image synthesis and segmentation,” 2018, doi: 10.1109/CVPRW.2018.00298.

[45] P. Goldsborough, N. Pawlowski, J. C. Caicedo, S. Singh, and A. E. Carpenter, “CytoGAN: Generative Modeling of Cell Images,” *bioRxiv*, 2017, doi: 10.1101/227645.

[46] P. Baniukiewicz, E. J. Lutton, S. Collier, and T. Bretschneider, “Generative Adversarial Networks for Augmenting Training Data of Microscopic Cell Images,” *Front. Comput. Sci.*, 2019, doi: 10.3389/fcomp.2019.00010.

[47] Y. Jing, Y. Yang, Z. Feng, J. Ye, Y. Yu, and M. Song, “Neural Style Transfer: A Review,” *IEEE Trans. Vis. Comput. Graph.*, 2020, doi: 10.1109/TVCG.2019.2921336.

[48] Y. Borisov, M. Kolomeichenko, and D. Drozdov, “Supervisely,” 2020. https://supervise.ly.

[49] Z. Wang, A. C. Bovik, H. R. Sheikh, and E. P. Simoncelli, “Image quality assessment: From error visibility to structural similarity,” *IEEE Trans. Image Process.*, 2004, doi: 10.1109/TIP.2003.819861.

[50] P. Kancharla and S. S. Channappayya, “Improving the Visual Quality of Generative Adversarial Network (GAN)-Generated Images Using the Multi-Scale Structural Similarity Index,” 2018, doi: 10.1109/ICIP.2018.8451296.

[51] H. Tang, D. Xu, W. Wang, Y. Yan, and N. Sebe, “Dual Generator Generative Adversarial Networks for Multi-domain Image-to-Image Translation,” 2019, doi: 10.1007/978-3-030-20887-5_1.

[52] D. Lee, J. Kim, W. J. Moon, and J. C. Ye, “Collagan: Collaborative gan for missing image data imputation,” 2019, doi: 10.1109/CVPR.2019.00259.

[53] M. Heusel, H. Ramsauer, T. Unterthiner, B. Nessler, and S. Hochreiter, “GANs trained by a two time-scale update rule converge to a local Nash equilibrium,” 2017.

[54] C. Reich, T. Prangemeier, C. Wildner, and H. Koeppl, “Multi-StyleGAN: Towards Image-Based Simulation of Time-Lapse Live-Cell Microscopy,” 2021, doi: 10.1007/978-3-030-87237-3_46.

[55] T. Zhang *et al.*, “SkrGAN: Sketching-rendering unconditional generative adversarial networks for medical image synthesis,” 2019, doi: 10.1007/978-3-030-32251-9_85.

[56] C. Szegedy, V. Vanhoucke, S. Ioffe, J. Shlens, and Z. Wojna, “Rethinking the Inception Architecture for Computer Vision,” 2016, doi: 10.1109/CVPR.2016.308.

[4] Erdem, Y. S., ÖZUYSAL, Ö. Y., Okvur, D. P., TÖREYİN, B. U., ÜNAY, D. (2021). An image segmentation method for wound healing assay images. *Natural and Applied Sciences Journal*, *4*(1), 30-37.

[5] Erdem, Y. S., IHEME, L. O., BALIKÇI, M., ÖZUYSAL, Ö. Y., TÖREYİN, B. U., ÜNAY, D. "A U-Net Based Structure for Segmentation of High-Resolution Wound Healing Assay Time-Series Images" In: International Graduate Research Symposium (IGRS'22), (2022): 2022, June 3.

[6] Erdem, Y. S., Ayanzadeh, A., Mayalı, B., Balıkçi, M., Belli, Ö. N., Uçar, M., Ünay, D. (2023). Automated analysis of phase-contrast optical microscopy time-lapse images: application to wound healing and cell motility assays of breast cancer. In *Diagnostic Biomedical Signal and Image Processing Applications with Deep Learning Methods* (pp. 137-154). Academic Press.

[7] Erdem, Y. S., ÖZUYSAL, Ö. Y., Okvur, D. P., TÖREYİN, B. U., ÜNAY, D. "Novel Neural Style Transfer Based Data Synthesis Method for Phase-Contrast Wound Healing Assay Images" Biomedical Signal Processing and Control (Under review)